JM PAPERS

The role of fluid–structure coupling in the generation of an attractive squeeze-film force

S. Ramanarayanan[1],† **and A.L. Sánchez**[1]

[1]Department of Mechanical and Aerospace Engineering, University of California San Diego, La Jolla, CA 92093-0411, USA

Developed in this study is a theoretical description of squeeze-film lubrication systems that involve the flexural oscillation of a thin plate near a parallel wall. Such systems were discovered in recent experiments to produce load-bearing attractive forces that are a thousandfold stronger than those generated by rigid oscillators, which typically favour repulsion. Analyses of squeeze-film gas flow driven by a presumed plate deformation reproduce the observed magnification of attractive load capacity, but exhibit serious discrepancies with crucial aspects of the experimental measurements – most importantly, the precise distribution of air pressure along the film. The discrepancies are resolved in this study by accounting for the presence of two-way-coupled fluid–structure interactions whereby the undulations of the plate, modelled here with use of the classical Kirchhoff–Love equation, are affected non-negligibly by the evolving pressure, described by a modified Reynolds lubrication equation that accounts for compressibility. The resulting problem of elastohydrodynamic lubrication is solved with use of perturbation methods that exploit the limit of small oscillation amplitudes. The analysis ultimately provides an explicit expression specifying the attractive load capacity of a squeeze-film system as a function of relevant operating parameters – including, in particular, the amplitude and frequency of the localized excitation force exerted on the plate. The rudimentary theory derived here may be readily generalized to guide the analysis and development of a wide variety of emerging engineering systems that exploit the vibration-induced squeeze-film effect – such as wall-climbing soft robots and contactless grippers.

Key words: flow-structure interactions, gas dynamics, lubrication theory

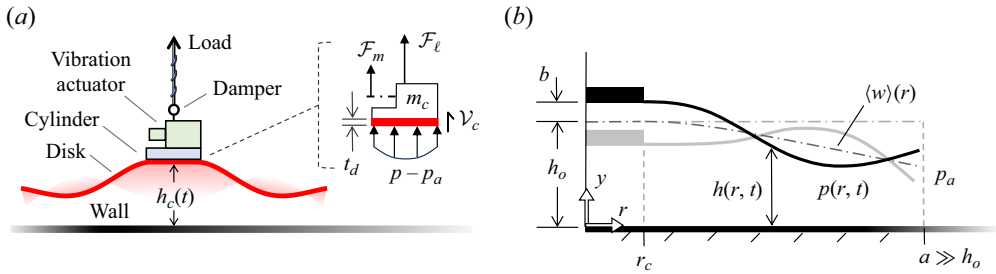† Email address for correspondence: sramanar@ucsd.edu

Figure 1. (*a*) Cartoon and free-body diagram of a load-bearing SFL system enabled by the flexural oscillation of a thin, locally excited disk and (*b*) a formal schematic of the axisymmetric system geometry used in the problem definition § 2.

1. Introduction

Colasante (2015) communicates an interesting experiment involving a flexible plate that is oscillated along its normal axis by an actuator affixed to its centre. When the plate is brought close to a non-adhesive parallel surface, it becomes subject to an attractive force that allows the exertion of a steady pulling load on the vibrating device, as depicted in figure 1(*a*). For example, when oscillating near a smooth concrete surface a square aluminium plate (with a thickness of 1 mm and a side length of 61 cm) at a frequency of 15 Hz, Colasante (2023) measures a load capacity of nearly 200 kgf (kilograms force) with a power consumption of $\approx$200 W (watts). The device exhibits remarkably low resistance to lateral motion (Colasante 2016), suggesting the presence of a lubricating layer of air that separates the undulating plate from the opposite surface.

In 2021, Weston-Dawkes *et al.* (2021) exploited this phenomenon (having arrived at it independently) in the design of a load-carrying robotic device capable of travelling underneath horizontal surfaces and up vertical walls with use of a standard wheel base and a thin, oscillating plastic disk. The device produced an attractive force exceeding 0.6 kgf using less than 0.3 W of power (Precision Microdrives 2021), thereby achieving an impressive operating efficiency of over 2 kgf W^{-1}. Subsequently, Jia *et al.* (2023) designed a robot that travelled and rotated controllably beneath a horizontal surface without the use of wheels. Instead, multiple vibration actuators were employed to excite travelling-wave deformations of the plate, the resulting streaming of air within the air layer providing propulsive/rotary shear stresses on the plate (Ramanarayanan & Sánchez 2023).

The phenomenon described above is commonly referred to as 'squeeze-film levitation' (SFL) (Shi *et al.* 2019), a method of gaseous lubrication discovered seemingly in the mid 1950s by which the required overpressure inside a wall-bounded gas layer is effectively provided by relative perpendicular oscillation of the walls (Taylor & Saffman 1957). In contrast to aerodynamic and aerostatic lubrication, which directly provide quasi-steady overpressures due to relative translational motion of non-parallel walls or external pumping of air, respectively, the oscillating pressure inside a squeeze film exhibits a cycle-averaged value that differs from the ambient value due to the nonlinear effects of gaseous compressibility and convective fluid acceleration (Melikhov *et al.* 2016; Ramanarayanan, Coenen & Sánchez 2022). The resulting pressure difference across the oscillating plate generates a time-averaged normal force that provides a steady load-bearing capacity.

Typical SFL systems involve highly stiff oscillators that are driven by bulky piezoelectric transducers at ultrasonic frequencies, and produce large repulsive forces
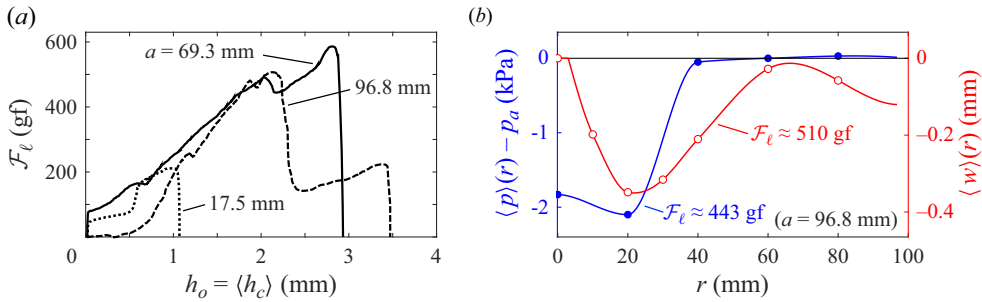
Figure 2. Approximate reproduction of selected experimental measurements by Weston-Dawkes *et al.* (2021): (*a*) variation of the applied pulling load with the mean central separation distance and (*b*) time-averaged radial distribution of the gauge pressure in the air layer $\langle p \rangle(r) - p_a$ (blue) along with the accompanying time-averaged deformation of the oscillating disk in relation to its mean central position $\langle w \rangle(r)$ (red) (see figure 1 for notation).

that render them suitable for conventional bearing lubrication. For example, Zhao (2010) measured a steady repulsive force of ≈ 11.7 kgf, with an operating efficiency of ≈ 0.24 kgf W^{-1}, by oscillating a cylindrical oscillator of diameter 5 cm at a frequency of 20 000 Hz. Prior to the experiments by Colasante (2015), attractive forces had been found to occur only under a limited range of operating conditions – relatively low frequencies or oscillators with small surface area, the corresponding load capacities being thousands of times weaker. For example, a maximal attractive force of just ≈ 0.5 gf (grams-force) was measured by Sadayuki (2002) using a cylindrical oscillator of diameter 7 cm and frequency 200 Hz. Correspondingly, throughout history, levitation and transportation/rotation systems enabled by repulsive forces have garnered considerable theoretical attention (Zhao 2010; Feng, Liu & Cheng 2015; Chen *et al.* 2016; Davis, Gabai & Bucher 2018; Guo & Gao 2018; Shi *et al.* 2019), while fewer studies have addressed the emergence of the much weaker attractive forces (Yoshimoto, Shou & Somaya 2013; Andrade *et al.* 2020; Ramanarayanan *et al.* 2022).

A recent theoretical study (Ramanarayanan & Sánchez 2022) posited that the impressive magnification of attractive load capacity and energy efficiency observed in the recent experiments by Colasante (2015) and Weston-Dawkes *et al.* (2021), which may conceivably expand the range of practical applications of SFL, can be attributed to the pronounced dynamic bending experienced by the highly flexible oscillators utilized. Through a rigorous analysis of the fluid-flow dynamics in the air layer and its immediate periphery, the authors proved that the attractive force provided by resonant flexural oscillation of a thin circular plate may be thousands of times greater than that provided by rigid-body oscillation under otherwise identical conditions – specifically, the same central displacement amplitude. However, the theoretical predictions of Ramanarayanan & Sánchez (2022) and the detailed experimental measurements provided by Weston-Dawkes *et al.* (2021) exhibit fundamental disagreements regarding crucial aspects of the underlying physics. For instance, while the experimental data show a gradual rise of the force to a maximal value as the cycle-averaged separation distance between the centre of the oscillating plate and the opposite wall is increased to a value of ≈ 1–3 mm, as exemplified in figure 2(*a*), the theory predicts a rapid growth of comparable magnitude as the distance is increased to values of order 50 μm. Furthermore, measurements show that the time-averaged gauge pressure in the air layer features a localized region of negative values at its centre, as exemplified in figure 2(*b*), while the theoretically predicted distribution varies gradually and always features a positive central value.

1001 A52-3

We argue in this paper that these fundamental differences may be attributed to the presence of two-way-coupled fluid–structure interactions in practical systems, whereby the dynamics of the flexible oscillator is affected non-negligibly by the overpressure generated in the air layer due to its motion. The effects of two-way coupling are demonstrably negligible in the case of the highly stiff oscillators used in earlier studies to generate repulsive forces (Li, Liu & Ding 2014). They are, however, palpable in the experiments of Weston-Dawkes *et al.* (2021), as evidenced by the observed cycle-averaged deformation of the thin plastic oscillator, exemplified in figure 2(*b*), which correlates closely with the associated distribution of the time-averaged overpressure pictured in the same panel. Fluid–structure coupling has been explored before in repulsive SFL configurations where a rigid body is levitated above an oscillating plate/piston. The influence of film pressure on the Newtonian dynamics of the levitated body has been studied in the case of rigid oscillators (Brunetière, Blouin & Kastane 2018) and those undergoing prescribed standing-wave deformations (Ilssar, Bucher & Flashner 2017). Ilssar & Bucher (2017) additionally explored effects of coupling on the displacement amplitude of a rigid oscillator. Zhang, Xu & Jiang (2004) and Pandey & Pratap (2007) elucidated the damping effect of viscous flow in the air layer on the resonant dynamic bending of a compliant plate. To the best of our knowledge, a theoretical investigation is yet to be conducted into the effects of two-way coupling on the time-averaged repulsive/attractive load capacity of an SFL system equipped with a flexible oscillator, that being the objective of the present study.

We formulate below in § 2 a reduced mathematical description of the compressible gas flow in a squeeze-film system driven by the flexural oscillation of a compliant plate, by application of the nonlinear theory of elastohydrodynamic lubrication (Sim & Kim 2008; Greenwood 2020; Wu *et al.* 2020; Poulain *et al.* 2022; Rallabandi 2024). The equations governing the fluid–structure dynamics are coupled with a statement of Newton's second law involving the sinusoidal excitation force exerted by the vibration actuator, and the resulting system of equations is solved approximately under the asymptotic limit of small oscillations. The leading-order analysis, presented in § 3, leads to an explicit expression relating the known forcing amplitude of excitation and the consequent displacement amplitude of material points on the oscillating plate. The nonlinear problem that emerges at the following asymptotic order is solved in § 4 to provide a concise analytical expression for the operating efficiency of a flexural SFL system: the ratio of the generated time-averaged force to the supplied excitation amplitude. Simplified forms of these expressions are derived in § 5 to describe centrally forced systems, as a singular limiting case of the general problem. Results of the asymptotic theory are verified in § 6 by comparison with finite-difference computations, and shown in §§ 6 and 7 to provide improved agreement with salient aspects of recently obtained experimental data. Finally, recommendations are provided in § 8 for further theoretical research that may inspire and inform future innovations that exploit this emerging technology.

2. Problem definition

2.1. *Modelling approach*

Represented in figures 1(*a*) and 1(*b*) are simplified schematics of the mechanical configuration involved in recent experiments where strong attractive forces were generated with an SFL system (Colasante 2016; Weston-Dawkes *et al.* 2021; Omodia, Das & Mahadevan 2022). A flexible disk of radius *a* and uniform thickness t_d is located near a parallel wall. Glued coaxially to the opposite surface of the disk is a rigid, circular

cylinder of radius $r_c < a$, to which a vibration actuator is affixed. The actuator exerts on the cylinder an oscillatory axial force that varies sinusoidally in time with frequency $\omega/(2\pi)$ (where ω denotes the associated angular frequency), causing the disk to undergo dynamic bending. The nonlinear dynamics of the oscillatory airflow excited in the air layer separating the disk and the wall (Ramanarayanan *et al.* 2022), the 'squeeze film', gives rise to a cycle-averaged pressure field in the film that provides a steady force attracting the disk toward the wall. This attractive force is able to support an applied pulling load of magnitude $\mathcal{F}_\ell$, steadied at the point of application by a vibration damper.

Application of Newton's second law for the rigid central assembly on which the load is exerted and the central portion of the disk to which it is affixed (see the inset in figure 1(*a*) for clarification) provides

$$\mathcal{F}_\ell + \mathcal{F}_m \cos(\omega t + \phi) + 2\pi \int_0^{r_c} (p - p_a) r \, dr + 2\pi r_c \mathcal{V}_c = (\pi r_c^2 \rho_d t_d + m_c)\frac{\partial^2 h_c}{\partial t^2}, \quad (2.1)$$

where t and r denote, respectively, the time and the radial distance from the axis of symmetry, $\mathcal{F}_m$ denotes the amplitude of the sinusoidal excitation force, $p(r, t) - p_a$ denotes the distributed gauge pressure acting on the disk surface (with p_a denoting the ambient pressure), $\mathcal{V}_c$ represents the axial structural stress resultant within the disk at the critical radius r_c, m_c quantifies the collective mass of the cylinder and other structures involved in the transfer of the vibrational force to the disk, ρ_d denotes the uniform density of the disk and $h_c(t)$ represents the time-varying distance between the wall and the central portion of the disk. The phase shift ϕ included in the argument of the excitation force is introduced to facilitate the analysis, and will be discussed later. In writing (2.1), the gravitational acceleration is assumed to be negligibly small in comparison with that induced by the high-frequency excitation, and the weight of the central assembly is assumed to be small relative to the steady pulling load, both assumptions being consistent with the operating conditions used by Weston-Dawkes *et al.* (2021).

Experimental data suggest that the central separation distance h_c fluctuates periodically about a constant mean value h_o if the imposed load $\mathcal{F}_\ell$ is steady. The mean distance h_o grows as the load is quasi-statically increased, until a critical value is reached beyond which the attractive force becomes insufficient and the disk detaches abruptly from the wall, as depicted in figure 2(*a*) (Weston-Dawkes *et al.* 2021). It is of great interest to devise a solution of (2.1) that allows prediction of the 'load capacity' of an SFL system, the maximal pulling force $max[\mathcal{F}_\ell(h_o)]$ that can be supported without failure. In practical systems, known quantities are typically limited to the structural properties of the disk, the thermodynamic properties of the operating fluid and the amplitude $\mathcal{F}_m$ and frequency of the excitation force (Burroughs 2021). Solution thus requires determining simultaneously the oscillating position $h_c(t)$ of the central assembly and the reactive aerodynamic and structural forces affecting its motion. The nonlinear fluid–structure dynamics involved complicates the solution, in that the periodic cylinder motion may exhibit multiple harmonics in addition to the excitation frequency ω.

As shown in the following derivation, the problem simplifies in the case of small axial displacements of the disk relative to the mean separation distance h_o, allowing approximate solution of (2.1) with use of classical perturbation methods. Under the limit of small relative amplitudes, the cylinder may be assumed in the first approximation to oscillate sinusoidally along its axis with a given amplitude $b \ll h_o$ – as indicated in figure 1(*b*) – and an angular frequency equal to that of the excitation force, so that

$$h_c = h_o + b \cos(\omega t). \quad (2.2)$$

Secondary frequencies arising from weak nonlinear dynamics will enter as asymptotic corrections to h_c/h_o of order $(b/h_o)^2 \ll 1$ and smaller, to be discussed later. As indicated in (2.1), the cylinder displacement (2.2) is expected to exhibit a phase lag ϕ with respect to the excitation force, which is affected non-negligibly by the dissipative effects of viscous stresses in the squeeze film and material friction within the disk (Bettini 2016). In general, the evolving width $h(r, t)$ of the film may be expressed with use of the function

$$w(r, t) = h - h_o, \tag{2.3}$$

which denotes the position of the disk surface bounding the air film. Since the central portion of the disk is glued to the cylinder, it follows from (2.2) that, in the first approximation,

$$w = b \cos(\omega t) \quad \text{for } 0 \leq r \leq r_c. \tag{2.4}$$

In pursuit of determining simultaneously the central oscillation amplitude b and the reactive forces modulating its value, we introduce below a reduced theoretical description of the relevant fluid–structure dynamics, which couples the Reynolds equation governing the variation of air pressure p in the squeeze film with the Kirchhoff–Love equation governing the dynamic displacement w of the flexible annular portion of the disk $r_c \leq r \leq a$. We show that, when $b/h_o \ll 1$, the coupled equations can be solved with use of (2.4) as the driving kinematic boundary condition to provide analytical expressions for the reactive forces in terms of b. Substituting these expressions in (2.1) allows straightforward computation of the value of b with relative errors of order $b/h_o \ll 1$. Solving the nonlinear system of equations that emerges at the following order in the asymptotic description for $b/h_o \ll 1$ allows analytical determination of the levitation force $\mathcal{F}_\ell$ with the same level of accuracy.

The asymptotic formulation will be shown below to provide promising agreement with experimental measurements of the pull-off curve $\mathcal{F}_\ell(h_o)$, the time-averaged overpressure in the squeeze film $\langle p \rangle(r) - p_a$ and the accompanying steady deformation of the disk $\langle w \rangle(r)$ (see figures 1(b) and 2 for clarification). Here, the angled brackets are used to denote the cycle-averaging operator

$$\langle * \rangle = \frac{\omega}{2\pi} \int_t^{t+2\pi/\omega} * \, \mathrm{d}t. \tag{2.5}$$

2.2. *Description of the squeeze-film gas dynamics*

In modelling the gas flow, it will be assumed that the squeeze film is slender, i.e. $h_o \ll \lambda$, with the characteristic flexural wavelength λ of the disk being comparable to its radius a. Additionally, the viscous time scale $h_o^2/(\mu_a/\rho_a)$, where μ_a and ρ_a denote respectively the ambient dynamic viscosity and density of the gas, is taken to be much smaller than the oscillation period $2\pi/\omega$, so that the momentum balance is dominated by viscous forces and the energy balance by transverse heat conduction (since the Prandtl number of air is of order unity (Rohsenow, Hartnett & Cho 1998, p. 2.4)). In this approximation, the gas temperature across the film equals that of the solid boundaries, which is assumed here to equal the ambient gas temperature. In the associated limit of isothermal lubrication theory, the gas flow is determined, with relative errors of order $(h_o/a)^2 \ll 1$ and $h_o^2 \omega/(\mu_a/\rho_a) \ll 1$,

by the familiar equations (Langlois 1962; Ramanarayanan *et al.* 2022)

$$\frac{\partial \rho}{\partial t} + \frac{1}{r}\frac{\partial(\rho r u)}{\partial r} + \frac{\partial(\rho v)}{\partial y} = 0, \quad \frac{\partial p}{\partial r} = \mu_a \frac{\partial^2 u}{\partial y^2}, \quad \frac{\partial p}{\partial y} = 0 \quad \text{and} \quad \frac{p}{\rho} = \frac{p_a}{\rho_a}, \quad (2.6a\text{--}d)$$

where y is the normal distance to the wall, u and v denote respectively the radial and axial components of the flow velocity and ρ and p denote respectively the variable gas density and pressure, the subscript 'a' denoting ambient values found in the unperturbed surroundings.

The flow velocity in the film must satisfy the no-slip condition $u = 0$ on both bounding surfaces $y = 0$ and $y = h$ as well as the corresponding no-penetration conditions given by $v = 0$ at $y = 0$ and $v = \partial w/\partial t$ at $y = h$. Note that the condition $u(y = h) = 0$ ignores negligibly small radial displacements of material points on the disk, of the order of $(b/h_o)^2 (h_o/a)^2 a \ll a$. The associated gas pressure must satisfy the conditions of regularity at the central axis of the film and relaxation at its edge

$$\partial p/\partial r = 0 \text{ at } r = 0 \quad \text{and} \quad p = p_a \text{ at } r = a, \quad (2.7a,b)$$

respectively, the latter of which neglects variations of pressure existing beyond the edge, which are negligibly small in the lubrication limit, as explained in Appendix A.

The problem defined above affords straightforward reduction to the single equation

$$\frac{\partial}{\partial t}[(h_o + w)p] - \frac{1}{12\mu_a r}\frac{\partial}{\partial r}\left[(h_o + w)^3 p r \frac{\partial p}{\partial r}\right] = 0, \quad (2.8)$$

the relevant Reynolds lubrication equation for compressible flow (Harrison 1913; Langlois 1962; Ramanarayanan *et al.* 2022), which relates the disk deformation $w(r, t) = h - h_o$ with the coupled film pressure $p(r, t)$, the latter independent of y, as follows from (2.6c). The evolving pressure is to be determined by integration of (2.8) subject to the boundary conditions (2.7). Solution requires knowledge of the disk position w, whose value for $0 \le r \le r_c$ is determined in the first approximation by the presumed cylinder motion, as stated in (2.4), while its unknown value in the annular region $r_c < r \le a$ must be obtained from an analysis of the disk structural dynamics, as described below.

2.3. *Description of the disk structural dynamics*

In analysing the oscillations of the deformable portion of the disk extending for $r_c \le r \le a$, it will be assumed that the disk is made of a homogeneous, isotropic material, and that its axial deflections, comparable in magnitude to the central amplitude b, are much smaller than its uniform thickness t_d, which in turn is much smaller than its radius a, i.e. $b \ll t_d \ll a$. The excitation frequency is assumed to be sufficiently low for the characteristic flexural wavelength λ of the disk to be comparable to the disk radius a, consistent with the slender-flow assumption drawn in § 2.2. Under these conditions the disk can be assumed to undergo pure bending (Timoshenko & Woinowsky-Krieger 1959, pp. 47–49), whence its dynamic deformations, influenced non-negligibly by the squeeze-film overpressure $p(r, t) - p_a$, can be described with use of the Kirchhoff–Love equation (Kelly 2013; Ducceschi 2014)

$$\mathcal{D}\bar{\nabla}^4 w + \rho_d t_d \frac{\partial^2 w}{\partial t^2} = p - p_a, \quad \text{where } \mathcal{D} = \frac{E_d t_d^3}{12(1 - \nu_d^2)}, \quad (2.9a,b)$$

involving the axisymmetric Laplacian operator $\bar{\nabla}^2 = [\partial^2/\partial r^2 + (1/r)\partial/\partial r]$ and the flexural rigidity $\mathcal{D}$ of the disk, the latter defined in terms of the disk Young's modulus

E_d, mass density ρ_d and Poisson's ratio ν_d. Correspondingly, the axial stress resultant $\mathcal{V}_c$ affecting the dynamics of the central assembly (2.1) can be expressed as (Yang 2005)

$$\mathcal{V}_c = -\mathcal{D}[\partial(\bar{\nabla}^2 w)/\partial r]_{r=r_c}. \tag{2.10}$$

Note that the displacement of the neutral plane of the disk has been substituted in (2.9a) and (2.10) with that of its film-adjacent surface w (2.3), introducing negligible relative errors of order $(b/h_o)(t_d h_o/a^2) \ll 1$. Also, in-plane stresses induced due to fluid shear acting on this surface (Timoshenko & Woinowsky-Krieger 1959, pp. 378–380) are smaller than the expected overpressure by a factor of order $(b/h_o)(h_o/a)^2 \ll 1$ (Watanabe & Hara 1997; Tulchinsky & Gat 2016) and, hence, neglected when writing (2.9a).

Equation (2.9a) must be integrated for $r_c \leq r \leq a$ with the four boundary conditions

$$\begin{cases} w - b\cos(\omega t) = \dfrac{\partial w}{\partial r} = 0 & \text{at } r = r_c \\[2mm] \left(\dfrac{\partial^2}{\partial r^2} + \dfrac{\nu_d}{r}\dfrac{\partial}{\partial r} \right) w = \dfrac{\partial}{\partial r}(\bar{\nabla}^2 w) = 0 & \text{at } r = a \end{cases}, \tag{2.11}$$

which state that the annular portion of the disk is clamped at its inner edge $r = r_c$, where it follows the driving motion of the cylinder (2.4), and that neither bending moments nor axisymmetric axial stresses are supported at its free outer edge $r = a$ (see Timoshenko & Woinowsky-Krieger 1959, pp. 83–84 and Yang 2005, pp. 840–841).

2.4. *Dimensionless formulation and governing parameters*

It is useful to reformulate the fluid–structure problem defined in §§ 2.2 and 2.3 in terms of appropriate dimensionless variables, beginning with the temporal and spatial variables $\tau = \omega t$ and $\xi = r/a$. The disk displacement is scaled with the central amplitude b to give $W(\xi, \tau) = w/b$. We may then use (2.3) to write $h/h_o = 1 + \varepsilon W$, where

$$\varepsilon = b/h_o \tag{2.12}$$

defines the relative central oscillation amplitude. It follows from (2.4) that, in the first approximation, $W = \cos \tau$ for $\xi \leq \xi_c$, where $\xi_c = r_c/a$ defines the dimensionless clamping radius. The characteristic scale of film overpressure, deduced readily from (2.6a,b) (see Appendix A), is used to define the variable $P = 12(p - p_a)/(\varepsilon \sigma p_a)$, where

$$\sigma = \frac{12\mu_a \omega a^2}{p_a h_o^2}, \tag{2.13}$$

the classical dimensionless 'squeeze number' (Langlois 1962), quantifies the degree of gaseous compressibility in the film induced by viscous retardation of radial airflow.

The Reynolds lubrication equation (2.8) can now be written in the dimensionless form

$$\sigma \frac{\partial}{\partial \tau}[(1 + \varepsilon W)P] - \frac{1}{\xi}\frac{\partial}{\partial \xi}\left[(1 + \varepsilon W)^3 \left(1 + \frac{\varepsilon \sigma}{12}P \right) \xi \frac{\partial P}{\partial \xi} \right] + 12\frac{\partial W}{\partial \tau} = 0, \tag{2.14}$$

while the Kirchhoff–Love equation (2.9a) takes the form

$$\nabla^4 W + K^4 \frac{\partial^2 W}{\partial \tau^2} = \mathcal{C}^6 P, \tag{2.15}$$

where $\nabla^2 = [\partial^2/\partial\xi^2 + (1/\xi)\partial/\partial\xi]$. As seen from (2.15), consideration of the disk dynamics introduces two additional dimensionless parameters defined by

$$K^4 = a^4\omega^2\frac{12\rho_d(1-\nu_d^2)}{E_d t_d^2} \quad \text{and} \quad \mathcal{C}^6 = a^6\frac{12\mu_a\omega(1-\nu_d^2)}{E_d(t_d h_o)^3}, \tag{2.16a,b}$$

where K represents the well-known elastic wavenumber characterizing the bending of an isolated disk, i.e. one for which $\mathcal{C} = 0$ (Warren 1930; Yang 2005; Ramanarayanan & Sánchez 2022). In the proceeding analysis, the ratio of the scale of film overpressure to that of disk inertia, $\mathcal{C}^6/K^4$, is found to be an important quantity that characterizes the 'degree' of flow–structure coupling. Interestingly, in the extreme case of strong coupling $\mathcal{C}^6/K^4 \gg 1$, the parameter K is found to disappear from the formulation and is replaced by $\mathcal{C}$ as the relevant flexural wavenumber.

As follows from (2.7), (2.14) must be integrated with the boundary conditions

$$\partial P/\partial\xi = 0 \text{ at } \xi = 0 \quad \text{and} \quad P = 0 \text{ at } \xi = 1, \tag{2.17}$$

while, based on (2.11), (2.15) must be integrated with

$$\begin{cases} W - \cos\tau = \partial W/\partial\xi = 0 & \text{at } \xi = \xi_c \\ \left(\dfrac{\partial^2}{\partial\xi^2} + \dfrac{\nu_d}{\xi}\dfrac{\partial}{\partial\xi}\right)W = \dfrac{\partial}{\partial\xi}(\nabla^2 W) = 0 & \text{at } \xi = 1 \end{cases}. \tag{2.18}$$

The problem defined above is to be addressed below for order-unity values of the distinguished dimensionless parameters σ, K and $\mathcal{C}$, in order to develop a unifying theoretical description that reconciles the remarkable recent discoveries with the well-understood physics of conventional SFL systems which, together, span a wide parametric range (see, for example, Salbu 1964; Hatanaka *et al.* 1999; Sadayuki 2002; Zhao 2010; Yoshimoto *et al.* 2013; Colasante 2015; Weston-Dawkes *et al.* 2021). Analytical progress will be made using classical asymptotic methods that exploit the limit of small relative amplitudes $\varepsilon = b/h_o \ll 1$, as similar historical approaches have afforded clear insights regarding the simplified physics of SFL configurations that feature extreme values of σ, K and/or $\mathcal{C}$ (Taylor & Saffman 1957; Langlois 1962; Ramanarayanan *et al.* 2022).

3. Leading-order dynamics for small relative amplitudes

We begin by expressing the dimensionless disk displacement and film overpressure as regular perturbation expansions of the forms $W = W_0 + \varepsilon W_1 + \cdots$ and $P = P_0 + \varepsilon P_1 + \cdots$, respectively. Substituting these expansions into the governing equations (2.14) and (2.15) and their boundary conditions (2.17) and (2.18), and collecting terms of order unity gives

$$\frac{\partial}{\partial\tau}(\sigma P_0 + 12W_0) - \nabla^2 P_0 = 0 \begin{cases} \xi = 0: & \partial P_0/\partial\xi = 0 \\ \xi = 1: & P_0 = 0 \end{cases}, \tag{3.1}$$

and

$$\nabla^4 W_0 + K^4\frac{\partial^2 W_0}{\partial\tau^2} = \mathcal{C}^6 P_0 \begin{cases} \xi = \xi_c: & W_0 - \cos\tau = \partial W_0/\partial\xi = 0 \\ \xi = 1: & \left(\dfrac{\partial^2}{\partial\xi^2} + \dfrac{\nu_d}{\xi}\dfrac{\partial}{\partial\xi}\right)W_0 = \dfrac{\partial}{\partial\xi}(\nabla^2 W_0) = 0 \end{cases}. \tag{3.2}$$

Since the motion of the central portion of the disk is prescribed at leading order by the uniform sinusoidal function $W_0 = \cos\tau$, as per (2.4), in seeking time-periodic solutions

of this linear problem it is convenient to introduce a piecewise-defined ansatz of the form

$$\left.\begin{array}{ll} P_0 = \mathrm{Re}\{\bar{\Pi}(\xi)\,\mathrm{e}^{\mathrm{i}\tau}\} \text{ and } W_0 = \mathrm{Re}\{\mathrm{e}^{\mathrm{i}\tau}\} & \text{for } 0 \leq \xi \leq \xi_c \\ P_0 = \mathrm{Re}\{\Pi(\xi)\,\mathrm{e}^{\mathrm{i}\tau}\} \text{ and } W_0 = \mathrm{Re}\{\Omega(\xi)\,\mathrm{e}^{\mathrm{i}\tau}\} & \text{for } \xi_c \leq \xi \leq 1 \end{array}\right\}, \tag{3.3}$$

where the complex spatial functions $\bar{\Pi}$, Π, and Ω are to be determined below.

In the central portion of the film $0 \leq \xi \leq \xi_c$, (3.1) reduces to $\bar{\Pi}'' + \bar{\Pi}'/\xi - \sigma\mathrm{i}\bar{\Pi} = 12\,\mathrm{i}$, where a prime superscript denotes the derivative of a spatial function, i.e. $f'(\xi) = \mathrm{d}f/\mathrm{d}\xi$. Integration with the regularity condition $\bar{\Pi}'(0) = 0$ gives the reduced pressure

$$\bar{\Pi} = (12\,\mathrm{i}/\varsigma^2)[1 + \bar{A}J_0(\varsigma\xi)], \quad \text{with } \varsigma = (1 - \mathrm{i})\sqrt{\sigma/2}, \tag{3.4}$$

where J_0 represents the Bessel function of the first kind of zeroth order, and the coefficient $\bar{A}$ is to be determined by patching the function $\bar{\Pi}$ (Bender & Orszag 1999, pp. 335–336) with the reduced pressure Π existing in the surrounding annular region $\xi_c \leq \xi \leq 1$.

In the annular region, we use (3.2) and (3.3) to write $\Pi = \mathcal{C}^{-6}(\nabla^4 - K^4)\Omega$, substitution of which in (3.1) yields the relevant 'thin-film' equation (Poulain *et al.* 2022)

$$\nabla^6\Omega - \sigma\mathrm{i}\nabla^4\Omega - K^4\nabla^2\Omega + \mathrm{i}(\sigma K^4 - 12\mathcal{C}^6)\Omega = 0. \tag{3.5}$$

The general solution to (3.5) can be written in the form

$$\Omega = \sum_{n=1}^{3}[A_nJ_0(\gamma_n\xi) + B_nY_0(\gamma_n\xi)], \tag{3.6}$$

whence the reduced pressure Π assumes the form

$$\Pi = \frac{1}{\mathcal{C}^6}\sum_{n=1}^{3}(\gamma_n^4 - K^4)[A_nJ_0(\gamma_n\xi) + B_nY_0(\gamma_n\xi)], \tag{3.7}$$

both involving the Bessel function of the second kind of zeroth order Y_0, the unknown coefficients A_n and B_n (where $n = 1 : 3$) and the constants γ_1, γ_2 and γ_3, defined by

$$\gamma_n^2 = -\frac{\mathrm{i}}{3}[\sigma + \mathrm{e}^{2\,\mathrm{i}\pi(n-1)/3}Q^{1/3} + (\sigma^2 - 3K^4)\,\mathrm{e}^{2\,\mathrm{i}\pi(1-n)/3}Q^{-1/3}], \quad \text{for } n = 1 : 3, \tag{3.8}$$

where

$$Q = \sigma^3 + 9\sigma K^4 - 162\mathcal{C}^6 - 3[3\,K^4(\sigma^2 + K^4)^2 + 36\mathcal{C}^6(81\mathcal{C}^6 - 9\sigma K^4 - \sigma^3)]^{1/2}. \tag{3.9}$$

The leading-order solution thus involves seven coefficients, $\bar{A}$, A_1, A_2, A_3, B_1, B_2 and B_3, to be determined by application of the five reduced boundary conditions

$$\begin{cases} \Omega - 1 = \Omega' = 0 & \text{at } \xi = \xi_c \\ \Pi = \Omega'' + v_d\Omega' = \Omega''' + \Omega'' - \Omega' = 0 & \text{at } \xi = 1 \end{cases}, \tag{3.10}$$

deduced from (3.1) and (3.2), and the two additional conditions $\bar{\Pi} = \Pi$ and $\bar{\Pi}' = \Pi'$ at $\xi = \xi_c$, which enforce continuity of the pressure and its gradient, respectively, at the interfacial clamp radius. The last condition guarantees continuity of the radial flow speed

1001 A52-10

$u \propto \partial p / \partial r$, evident from the radial momentum balance (2.6*b*), and involves the reduced pressure gradients in the central and annular regions

$$\bar{\Pi}' = -\frac{12\,\mathrm{i}}{\varsigma}\bar{A}J_1(\varsigma\xi) \quad \text{and} \quad \Pi' = \frac{1}{\mathcal{C}^6}\sum_{n=1}^{3}\gamma_n(K^4 - \gamma_n^4)[A_n J_1(\gamma_n\xi) + B_n Y_1(\gamma_n\xi)],$$

(3.11*a,b*)

respectively. Application of these seven conditions with use of (3.6) and (3.7) provides

$$\begin{bmatrix} \bar{A} & A_1 & B_1 & A_2 & B_2 & A_3 & B_3 \end{bmatrix} = \begin{bmatrix} 1 & 0 & 12\,\mathrm{i}\mathcal{C}^6/\varsigma^2 & 0 & 0 & 0 & 0 \end{bmatrix}\boldsymbol{M}^{-1}, \quad (3.12)$$

where $\boldsymbol{M}^{-1}$ represents the inverse of the square matrix

$$\boldsymbol{M} = \begin{bmatrix} 0 & 0 & \dfrac{12\mathcal{C}^6 J_0(\varsigma\xi_c)}{\mathrm{i}\varsigma^2} & \dfrac{12\,\mathrm{i}\mathcal{C}^6 J_1(\varsigma\xi_c)}{\varsigma} & 0 & 0 & 0 \\ J_0(\gamma_1\xi_c) & \gamma_1 J_1(\gamma_1\xi_c) & \Phi_J(\gamma_1,\xi_c) & \Psi_J(\gamma_1,\xi_c) & \Phi_J(\gamma_1,1) & \Theta_J(\gamma_1,1) & \gamma_1^3 J_1(\gamma_1) \\ Y_0(\gamma_1\xi_c) & \gamma_1 Y_1(\gamma_1\xi_c) & \Phi_Y(\gamma_1,\xi_c) & \Psi_Y(\gamma_1,\xi_c) & \Phi_Y(\gamma_1,1) & \Theta_Y(\gamma_1,1) & \gamma_1^3 Y_1(\gamma_1) \\ J_0(\gamma_2\xi_c) & \gamma_2 J_1(\gamma_2\xi_c) & \Phi_J(\gamma_2,\xi_c) & \Psi_J(\gamma_2,\xi_c) & \Phi_J(\gamma_2,1) & \Theta_J(\gamma_2,1) & \gamma_2^3 J_1(\gamma_2) \\ Y_0(\gamma_2\xi_c) & \gamma_2 Y_1(\gamma_2\xi_c) & \Phi_Y(\gamma_2,\xi_c) & \Psi_Y(\gamma_2,\xi_c) & \Phi_Y(\gamma_2,1) & \Theta_Y(\gamma_2,1) & \gamma_2^3 Y_1(\gamma_2) \\ J_0(\gamma_3\xi_c) & \gamma_3 J_1(\gamma_3\xi_c) & \Phi_J(\gamma_3,\xi_c) & \Psi_J(\gamma_3,\xi_c) & \Phi_J(\gamma_3,1) & \Theta_J(\gamma_3,1) & \gamma_3^3 J_1(\gamma_3) \\ Y_0(\gamma_3\xi_c) & \gamma_3 Y_1(\gamma_3\xi_c) & \Phi_Y(\gamma_3,\xi_c) & \Psi_Y(\gamma_3,\xi_c) & \Phi_Y(\gamma_3,1) & \Theta_Y(\gamma_3,1) & \gamma_3^3 Y_1(\gamma_3) \end{bmatrix},$$

(3.13)

expressed here in terms of the auxiliary functions

$$\left.\begin{aligned} \Phi_{\mathcal{B}}(\gamma_n,\xi) &= (\gamma_n^4 - K^4)\mathcal{B}_0(\gamma_n\xi) \\ \Psi_{\mathcal{B}}(\gamma_n,\xi) &= \gamma_n(K^4 - \gamma_n^4)\mathcal{B}_1(\gamma_n\xi) \\ \Theta_{\mathcal{B}}(\gamma_n,\xi) &= \gamma_n^2\left[\mathcal{B}_0(\gamma_n\xi) - \frac{1-\nu_d}{\gamma_n\xi}\mathcal{B}_1(\gamma_n\xi)\right] \end{aligned}\right\}, \quad (3.14)$$

where $\mathcal{B}_m$ represents a Bessel function of the first/second kind (J_m or Y_m) of mth order.

3.1. *Solving for the presumed displacement amplitude b*

The reactive aerodynamic and structural forces affecting the oscillation of the central assembly can now be expressed, with errors of order $\varepsilon \ll 1$, in the dimensionless forms

$$\frac{\displaystyle\int_0^{r_c}(p-p_a)r\,\mathrm{d}r}{\varepsilon p_a a^2} = -\mathrm{Re}\{F_c\,\mathrm{e}^{\mathrm{i}\tau}\}, \quad \text{where } F_c = \xi_c\left[\frac{\xi_c}{2} + \frac{\bar{A}}{\varsigma}J_1(\varsigma\xi_c)\right], \quad (3.15)$$

and, based on (2.10),

$$\frac{r_c\mathcal{V}_c}{\mathcal{D}b/a^2} = -\mathrm{Re}\{V_c\,\mathrm{e}^{\mathrm{i}\tau}\}, \quad \text{where } V_c = \xi_c\sum_{n=1}^{3}\gamma_n^3[A_n J_1(\gamma_n\xi_c) + B_n Y_1(\gamma_n\xi_c)], \quad (3.16)$$

respectively. Substituting into the governing equation of motion (2.1) the presumed central displacement (2.4), the central pressure force (3.15) and the structural impedance (3.16) reveals a linear relationship between the unknown displacement amplitude b and the (generally) known excitation amplitude $\mathcal{F}_m$, given by

$$\frac{b}{\mathcal{F}_m} = |\mathcal{X}|^{-1}, \quad \text{where } \mathcal{X} = 2\pi\left(\frac{a^2}{h_o}p_a F_c + \frac{\mathcal{D}}{a^2}V_c\right) - \omega^2(m_c + \pi r_c^2\rho_d t_d) \quad (3.17)$$

and an absolute value denotes the modulus of a complex quantity. The associated phase difference ϕ is given simply by $\phi = \arg(\mathcal{X})$. Note that this estimate for the value of b,

accurate with relative errors of order $\varepsilon = b/h_o \ll 1$, does not require knowledge of the load $\mathcal{F}_\ell$ which enters in (2.1) as an asymptotic correction of order ε.

4. Time-averaged behaviour at first order

The disk displacement at leading order, W_0, and the associated film overpressure, P_0, both vary sinusoidally with time and thus exhibit a zero time average, i.e. $\langle W_0 \rangle = \langle P_0 \rangle = 0$, the angled brackets denoting the cycle-averaging operator (2.5). Determining the steady pressure distribution and the steady disk deformation thus requires solving the problem that emerges at the following asymptotic order. Collecting terms of order ε in the expanded forms of (2.14) and (2.15) and their boundary conditions (2.17) and (2.18), and computing the cycle average thereof, provides the system of equations

$$\frac{\partial}{\partial \xi} \left[\xi \left(3 \left\langle W_0 \frac{\partial P_0}{\partial \xi} \right\rangle + \frac{\sigma}{24} \frac{\partial \langle P_0^2 \rangle}{\partial \xi} + \frac{\partial \langle P_1 \rangle}{\partial \xi} \right) \right] = 0 \begin{cases} \xi = 0 : & \partial \langle P_1 \rangle / \partial \xi = 0 \\ \xi = 1 : & \langle P_1 \rangle = 0 \end{cases} \quad (4.1)$$

and

$$\nabla^4 \langle W_1 \rangle = \mathcal{C}^6 \langle P_1 \rangle \begin{cases} \xi = \xi_c : & \langle W_1 \rangle = \mathrm{d} \langle W_1 \rangle / \mathrm{d} \xi = 0 \\ \xi = 1 : & \left(\dfrac{\mathrm{d}^2}{\mathrm{d} \xi^2} + \dfrac{\nu_d}{\xi} \dfrac{\mathrm{d}}{\mathrm{d} \xi} \right) \langle W_1 \rangle = \dfrac{\mathrm{d}}{\mathrm{d} \xi} \left(\nabla^2 \langle W_1 \rangle \right) = 0 \end{cases}, \quad (4.2)$$

where the steady overpressure $\langle P_1 \rangle$ at the film edge $\xi = 1$ is negligibly small in the lubrication limit considered here, as explained in Appendix A, and the value of $\langle W_1 \rangle$ vanishes at the clamp radius $\xi = \xi_c$ since the driving cylinder oscillates about a constant mean position, as described below (2.1). In this connection, note from (4.1) and (4.2) that any secondary frequencies exhibited by $W_1(\xi, \tau)$ due to nonlinear first-order interactions are irrelevant when solving for the time-averaged quantities of present interest.

4.1. *Time-averaged squeeze-film overpressure and disk deformation*

The steady pressure distribution $\langle P_1 \rangle(\xi)$, independent of the steady disk deformation $\langle W_1 \rangle(\xi)$ under the present perturbative formulation, can be determined by straightforward integration of (4.1) to give

$$\langle P_1 \rangle(\xi) = 3 \int_\xi^1 \left\langle W_0 \frac{\partial P_0}{\partial \xi} \right\rangle(x) \, \mathrm{d}x - \frac{\sigma}{24} \langle P_0^2 \rangle, \quad (4.3)$$

where x serves as a dummy integration variable. Substitution of the expressions given in (3.3) provides

$$\langle P_1 \rangle = \begin{cases} \dfrac{1}{2} \mathrm{Re} \left\{ 3 \left[\bar{\Pi}(\xi_c) - \bar{\Pi}(\xi) + \displaystyle\int_{\xi_c}^1 \Pi'^*(x) \Omega(x) \mathrm{d}x \right] - \dfrac{\sigma}{24} \bar{\Pi} \bar{\Pi}^* \right\} & 0 \leq \xi \leq \xi_c \\ \dfrac{1}{2} \mathrm{Re} \left\{ 3 \displaystyle\int_\xi^1 \Pi'^*(x) \Omega(x) \mathrm{d}x - \dfrac{\sigma}{24} \Pi \Pi^* \right\} & \xi_c \leq \xi \leq 1 \end{cases}, \quad (4.4)$$

having made use of the identity $\langle \mathrm{Re}\{\mathcal{G} e^{\mathrm{i}\tau}\} \mathrm{Re}\{\mathcal{H} e^{\mathrm{i}\tau}\} \rangle = \mathrm{Re}\{\mathcal{G}^* \mathcal{H}\}/2$, where $\mathcal{G}$ and $\mathcal{H}$ are complex spatial functions and an asterisk denotes a complex conjugate.

Integration of (4.2) provides the accompanying time-averaged deformation of the disk

$$\langle W_1 \rangle = \mathcal{C}^6 \left(\mathcal{I}_1(\xi_c) \ln\left(\frac{\xi_c}{\xi}\right) + \frac{1}{64} \int_{\xi_c}^{\xi} x^4 [4\ln(x) - 5] \langle P_1 \rangle'(x) \, \mathrm{d}x \right.$$

$$- \frac{\ln(\xi)}{16} \int_{\xi_c}^{\xi} x^4 \langle P_1 \rangle'(x) \, \mathrm{d}x + \left. \vphantom{\int} \right|_{\xi_c}^{\xi} \mathcal{I}_2(\xi)$$

$$+ \left. \frac{\xi_c^2 [1 + 2\ln(\xi/\xi_c)] - \xi^2}{2[\xi_c^2 - 1 + 2/(1 - \nu_d)]} \left[\mathcal{I}_1(\xi_c) + \frac{1}{16} \int_{\xi_c}^{1} x^4 \langle P_1 \rangle'(x) \, \mathrm{d}x \right] \right) \quad (4.5)$$

expressed here in terms of the radial pressure gradient

$$\langle P_1 \rangle' = \frac{\mathrm{d}\langle P_1 \rangle}{\mathrm{d}\xi} = \begin{cases} -\dfrac{1}{2}\mathrm{Re}\left\{ \bar{\Pi}'^* \left(3 + \dfrac{\sigma}{12}\bar{\Pi} \right) \right\} & 0 \le \xi \le \xi_c \\[12pt] -\dfrac{1}{2}\mathrm{Re}\left\{ \Pi'^* \left(3\Omega + \dfrac{\sigma}{12}\Pi \right) \right\} & \xi_c \le \xi \le 1 \end{cases}, \quad (4.6)$$

and the auxiliary integral functions

$$\left. \begin{aligned} \mathcal{I}_1(\xi) &= \frac{\xi^2}{4} \left[\frac{\xi^2}{4} \langle P_1 \rangle + \ln(\xi) \int_{\xi}^{1} x^2 \langle P_1 \rangle'(x) \, \mathrm{d}x - \int_{\xi}^{1} x^2 \ln(x) \langle P_1 \rangle'(x) \, \mathrm{d}x \right] \\ \mathcal{I}_2(\xi) &= \frac{\xi^2}{16} \left[\frac{\xi^2}{4} \langle P_1 \rangle + [2\ln(\xi) - 1] \int_{\xi}^{1} x^2 \langle P_1 \rangle'(x) \, \mathrm{d}x - 2 \int_{\xi}^{1} x^2 \ln(x) \langle P_1 \rangle'(x) \, \mathrm{d}x \right] \end{aligned} \right\}. \tag{4.7}$$

4.2. *An analytical expression for the levitation force*

Consistent with the simplified description of gas dynamics presented in § 2.2, the steady, attractive squeeze-film levitation force can be expressed as $\mathcal{F}_\ell = -2\pi \int_0^a \langle p - p_a \rangle \, r\mathrm{d}r$, which follows from a cycle-averaged statement of Newton's second law for the periodically oscillating system cartooned in figure 1(*a*), comprising both the central assembly and the annular portion of the disk. (This definition for $\mathcal{F}_\ell$ may be obtained also by integrating the Kirchhoff–Love equation (2.9*a*) across the annular portion of the disk $r_c \le r \le a$, substituting the resulting expression for the stress resultant $\mathcal{V}_c$ (2.10) into the equation of motion (2.1) and taking the time average thereof.)

Based on the scalings introduced in § 2.4, the force $\mathcal{F}_\ell$ can be normalized with the supplied excitation amplitude $\mathcal{F}_m$ and the resulting relative oscillation amplitude $\varepsilon = b/h_o$ to provide a dimensionless expression for the operating efficiency of the system

$$\frac{\mathcal{F}_\ell}{\varepsilon \mathcal{F}_m} = \frac{\pi \mu_a \omega a^4}{h_o^3} \frac{\langle F_L \rangle}{|\mathcal{X}|}, \quad \text{where } \langle F_L \rangle = \frac{12 \mathcal{F}_\ell}{\varepsilon^2 \sigma p_a \pi a^2} = -2 \int_0^1 \langle P_1 \rangle \xi \, \mathrm{d}\xi \qquad (4.8a,b)$$

and the complex constant $\mathcal{X}$ is defined in (3.17). Integration by parts in (4.8*b*) yields $\langle F_L \rangle = \int_0^1 \xi^2 \langle P_1 \rangle' \, \mathrm{d}\xi$, wherein substitution of the steady pressure gradient (4.6) provides

$$\langle F_L \rangle = -\frac{1}{2}\mathrm{Re}\left\{ \frac{12}{\sigma}\bar{A}^* \left(\frac{2\xi_c}{\varsigma^*} [2J_1(\varsigma^*\xi_c) - \varsigma^*\xi_c J_0(\varsigma^*\xi_c)] - \varsigma^*\bar{A}\mathcal{I}_{JJ}(\xi_c; \varsigma, \varsigma^*) \right) \right.$$

$$+ \left. \sum_{n=1}^{3} \sum_{m=1}^{3} \frac{\gamma_n^*(K^4 - \gamma_n^{*4})}{\mathcal{C}^6} \left[3 + \frac{\sigma(\gamma_m^4 - K^4)}{12\mathcal{C}^6} \right] \right|_{\xi_c}^{1} \mathcal{I}_L(\xi) \right\}, \qquad (4.9)$$

involving the auxiliary function

$$\mathcal{I}_L(\xi) = A_m A_n^* \mathcal{I}_{JJ}(\xi; \gamma_m, \gamma_n^*) + A_m B_n^* \mathcal{I}_{JY}(\xi; \gamma_m, \gamma_n^*)$$
$$+ B_m A_n^* \mathcal{I}_{YJ}(\xi; \gamma_m, \gamma_n^*) + B_m B_n^* \mathcal{I}_{YY}(\xi; \gamma_m, \gamma_n^*), \tag{4.10}$$

and the four operators $\mathcal{I}_{JJ}, \mathcal{I}_{JY}, \mathcal{I}_{YJ}$ and $\mathcal{I}_{YY}$, defined collectively by

$$\mathcal{I}_{FG}(\xi; \beta_F, \beta_G) = 2\beta_G \xi [\beta_G F_0(\beta_F \xi) G_1(\beta_G \xi) - \beta_F F_1(\beta_F \xi) G_0(\beta_G \xi)]/(\beta_F^2 - \beta_G^2)^2$$
$$+ \xi^2 [\beta_G F_0(\beta_F \xi) G_0(\beta_G \xi) + \beta_F F_1(\beta_F \xi) G_1(\beta_G \xi)]/(\beta_F^2 - \beta_G^2), \tag{4.11}$$

where each F_m and G_m represents a Bessel function of the first or second kind (J_m or Y_m) of mth order (Rosenheinrich 2019, p. 301).

5. Simplified expressions describing centrally forced systems: $\xi_c \to 0$

Of particular interest in understanding the flow–structure physics of SFL systems is the problem of a disk that is subject to a concentrated load at its centre, experiencing internal structural stresses that grow unboundedly ($\propto r^{-1}$) near its axis $r = 0$. Warren (1930) approached this singular problem by analysing the undamped oscillation of an annular disk and considering the limit of a vanishing inner radius. Following this strategy, the general formulation developed in §§ 2–4 is exploited below to derive simplified expressions, independent of ξ_c, that describe the performance of a centrally forced system.

In the corresponding limit $\xi_c \to 0$, the regularity condition $\partial P/\partial \xi = 0$ for the pressure in the air layer may be applied directly at the clamp radius $\xi = \xi_c$. The constant coefficients that determine at leading order the annular pressure distribution P_0 (3.7) and disk flexure W_0 (3.6) can be expressed as $\lim_{\xi_c \to 0}[A_1\,B_1\,A_2\,B_2\,A_3\,B_3] = [1\,0\,0\,0\,0\,0]\boldsymbol{M}_0^{-1}$, in terms of the reduced matrix $\boldsymbol{M}_0 = [\boldsymbol{U}_1 \boldsymbol{U}_2\,\boldsymbol{U}_3]^{\mathrm{T}}$, where

$$\boldsymbol{U}_n = \begin{bmatrix} 1 & 0 & 0 & \Phi_J(\gamma_n, 1) & \Theta_J(\gamma_n, 1) & \gamma_n^3 J_1(\gamma_n) \\ 2\ln(\gamma_n)/\pi & 1 & \gamma_n^4 & \Phi_Y(\gamma_n, 1) & \Theta_Y(\gamma_n, 1) & \gamma_n^3 Y_1(\gamma_n) \end{bmatrix} \quad \text{for } n = 1:3. \tag{5.1}$$

Assuming a massless central assembly ($m_c = 0$), the complex constant $\mathcal{X}$ defined in (3.17) reduces here to $\lim_{\xi_c \to 0} \mathcal{X} = -4(\mathcal{D}/a^2)(B_1\gamma_1^2 + B_2\gamma_2^2 + B_3\gamma_3^2)$, whence the amplitude of the reactive forces affecting the central dynamics (2.1) can be expressed as

$$\lim_{\xi_c \to 0} |V_c| = \lim_{\xi_c \to 0} \frac{\mathcal{F}_m}{2\pi \mathcal{D} b/a^2} = \frac{2}{\pi} \left| \sum_{n=1}^{3} B_n \gamma_n^2 \right|. \tag{5.2}$$

The time-averaged overpressure $\langle P_1 \rangle(\xi)$ that emerges as a first-order correction is described by the second branch of the piecewise-defined equation (4.4), while the general expression (4.5) describing the resulting disk deformation $\langle W_1 \rangle(\xi)$ simplifies here to give

$$\lim_{\xi_c \to 0} \langle W_1 \rangle = \mathcal{C}^6 \left(\frac{1}{64} \int_0^\xi x^4 [4\ln(x) - 5] \langle P_1 \rangle'(x)\,\mathrm{d}x - \frac{\ln(\xi)}{16} \int_0^\xi x^4 \langle P_1 \rangle'(x)\,\mathrm{d}x \right.$$
$$\left. + \mathcal{I}_2(\xi) - \frac{\xi^2(1 - \nu_d)}{32(1 + \nu_d)} \int_0^1 x^4 \langle P_1 \rangle'(x)\,\mathrm{d}x \right), \tag{5.3}$$

both valid only for $0 < \xi \leq 1$. The levitation force (4.9) correspondingly reduces to

$$\lim_{\xi_c \to 0} \langle F_L \rangle = -\frac{1}{2} \mathrm{Re} \left\{ \sum_{n=1}^{3} \sum_{m=1}^{3} \frac{\gamma_n^*(K^4 - \gamma_n^{*4})}{\mathcal{C}^6} \left[3 + \frac{\sigma(\gamma_m^4 - K^4)}{12\mathcal{C}^6} \right] [\mathcal{I}_L(1) - \mathcal{I}_c] \right\}, \quad (5.4)$$

where

$$\mathcal{I}_c = \frac{4/\pi}{\gamma_m^2 - \gamma_n^{*2}} \left[\frac{\gamma_n^*(B_m A_n^* - A_m B_n^*)}{\gamma_m^2 - \gamma_n^{*2}} + \frac{B_m B_n^*}{\pi \gamma_n^*} \left(1 - \frac{2\ln(\gamma_m/\gamma_n^*)}{(\gamma_m/\gamma_n^*)^2 - 1} \right) \right]. \quad (5.5)$$

Combining (5.4) with (5.2) yields a reduced expression for the levitation efficiency

$$\lim_{\xi_c \to 0} \frac{\mathcal{F}_\ell}{\varepsilon \mathcal{F}_m} = \frac{\mathcal{C}^6}{2} \frac{\lim_{\xi_c \to 0} \langle F_L \rangle}{\lim_{\xi_c \to 0} |V_c|}. \quad (5.6)$$

6. Effects of two-way coupling on the flow–structure dynamics

The fluid–structure problem addressed above is governed by five principal dimensionless parameters as detailed in § 2.4: the perturbation parameter $\varepsilon = b/h_o \ll 1$, which compares the oscillation amplitude of the disk centre with its mean separation distance from the wall, the relative clamp radius $\xi_c = r_c/a$ beyond which the disk is allowed to bend (see figure 1b), the squeeze number σ, which quantifies the strength of viscous forces retarding airflow in the film and giving rise to compressibility, the elastic wavenumber K, which correlates inversely with the flexural wavelength of the disk anticipated based on its structural properties, and a coupling parameter $\mathcal{C}$, which measures the influence of pressure variations in the squeeze film on the disk deformations. Of greatest interest here are the final parameters σ, K and $\mathcal{C}$ which govern the fundamental fluid–structure dynamics, to be investigated below by focusing mainly on centrally excited configurations, i.e. those involving infinitesimally small values of ξ_c (see § 5). In the dimensionless computations presented below, the Poisson's ratio of the disk ν_d is assigned a value of 0.3, characteristic approximately of most plastic and metallic materials of relevance here (The Engineering ToolBox 2008; Sonelastic n.d.).

6.1. *System dynamics under one-way coupling*

The general formulation derived above simplifies in the limit $\mathcal{C} \to 0$ to describe one-way-coupled systems, as detailed in Appendix B. It is worth reviewing here the widely studied behaviour of such systems – those for which the oscillations of the disk are unaffected by the squeeze-film overpressure and, hence, the flow–structure physics is governed purely by the parameters σ and K. An increase in $\sigma \propto \omega a^2/h_o^2$, realized commonly by reducing the separation distance h_o, is known to result in a magnification of the typically repulsive squeeze-film force $\mathcal{F}_\ell < 0$ in a manner proportional to the inverse square of h_o (Taylor & Saffman 1957; Zhao 2010). This magnification is found to occur regardless of the flexibility of the oscillator (Li *et al.* 2014), the latter quantified by the elastic wavenumber K. A transition to attractive forces $\mathcal{F}_\ell > 0$ is found to occur for systems with sufficiently low frequency ω (Sadayuki 2002) and/or oscillator size a (Yoshimoto *et al.* 2013; Andrade *et al.* 2020). For these systems, attraction emerges only beyond a critical separation distance h_o, i.e. below a critical value of σ.

The range of operating conditions ω and a for which attraction can be found, as well as the resulting attractive load capacity, are found to depend strongly on the waveform exhibited by the oscillating disk (Ramanarayanan & Sánchez 2022). In the
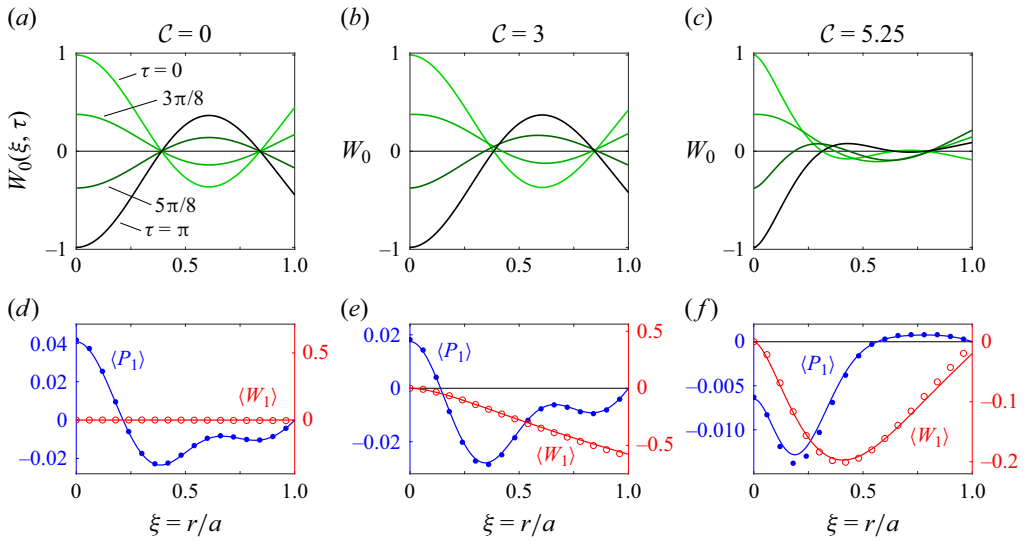
Figure 3. Behaviour of an SFL system operating with an elastic wavenumber of $K = 6.2$ and a squeeze number of $\sigma = 20$. The flexural disk oscillations that occur under (a) a state of one-way coupling ($\mathcal{C} = 0$) are juxtaposed with those that occur for states of (b) moderate two-way coupling ($\mathcal{C} = 3$) and (c) strong two-way coupling ($\mathcal{C} > 5$). Shown below in (d–f) are the associated radial distributions of time-averaged pressure and disk displacement. Dots and circles in (d–f) represent numerical solutions computed for $\varepsilon = 0.1$.

case of rigid-body oscillation, i.e. $K = 0$, repulsive forces exist for nearly all values of σ (Zhao 2010). Attractive forces can be produced under a very limited range of operating conditions, characterization of which requires modelling the effects of fluid inertia that are neglected in the lubrication approximation drawn in the present study, but the corresponding load capacities are several thousandfold smaller and, thus, of limited practical utility (Yoshimoto *et al.* 2013; Andrade *et al.* 2020). (Analysis of such conditions requires considering separately the contributions of fluid compressibility and inertia with use of the relevant acoustic wavenumber $K_a = a\omega/\sqrt{p_a/\rho_a}$ and the Womersley number $\alpha = [h_o^2\omega/(\mu_a/\rho_a)]^{1/2}$, which compare with the oscillation period the time scales of lateral pressure equilibration and transverse viscous diffusion, respectively. These two parameters enter implicitly in the present lubrication limit $\alpha^2 \ll 1$ through the single squeeze number $\sigma = 12K_a^2/\alpha^2$ (Melikhov *et al.* 2016; Ramanarayanan *et al.* 2022).) In contrast, for critical values of K that correspond to the natural frequencies of the disk (see Appendix B), the disk performs resonant standing-wave oscillations, such as those depicted in figure 3(a), and produces powerful attractive forces for a substantial range of values of σ (Ramanarayanan & Sánchez 2022). Note that excitation of the disk at a non-natural frequency may result in different flexural waveforms that, instead, only magnify the repulsive squeeze-film force. This is often seen in practical systems where the disk is affixed to a Piezoelectric transducer of much greater mass (Da Silva 1980; Li *et al.* 2014), yielding a mechanical assembly whose optimal, resonant frequencies presumably differ substantially from the native resonant frequencies of the disk.

Motion of a centrally excited disk at its second resonant mode, i.e. $K \approx 6.2$, is visualized in figure 3(a) for a value of the squeeze number $\sigma = 20$ that gives rise to an attractive force. As seen from the blue curve in figure 3(d), the distribution of steady pressure generated along the gas layer features two local minima whose radial locations correspond closely

with those of the two nodal circles in the standing flexural wave, $r/a \approx 0.4$ and 0.8. In the absence of aerodynamic forcing, the disk oscillates sinusoidally about an undeformed mean position, as indicated by the red line in figure 3(*d*). While this one-way-coupled description has been shown (Ramanarayanan & Sánchez 2022) to successfully reproduce the magnification of attractive load capacity found in flexural SFL systems (Colasante 2015; Weston-Dawkes *et al.* 2021), the predicted distribution of the causal time-averaged overpressure exhibits glaring disagreement with that measured in experiments, the latter exemplified in figure 2(*b*). Furthermore, setting $\mathcal{C} = 0$ precludes characterization of the accompanying time-averaged deformation of the disk, a sample measurement of which is also reproduced in figure 2(*b*). Accounting for two-way fluid–structure coupling by considering non-zero values of $\mathcal{C}$ yields greatly improved agreement with these observations, as described below.

6.2. *System dynamics under two-way coupling*

As seen from figures 3(*b*) and 3(*e*), increasing the value of the coupling parameter to $\mathcal{C} = 3$ yields but minor deviation from the one-way-coupled dynamics depicted in figures 3(*a*) and 3(*d*). The two nodal points are slightly disturbed and give way to localized regions of minimal amplitude, symptomatic of a damped oscillator (Geist & McLaughlin 1994). The corresponding steady pressure distribution $\langle P_1 \rangle (\xi)$ is visibly skewed but maintains a similar fundamental shape, and the disk oscillates about an approximately linearly deformed mean shape $\langle W_1 \rangle (\xi)$. Much more pronounced changes are observed when the strength of the aerodynamic forcing is further increased by setting $\mathcal{C} = 5.25$, for which value the disk exhibits travelling-wave-type oscillations whose amplitude is suppressed severely beyond $r/a \approx 0.3$, as shown in figure 3(*c*). As seen from figure 3(*f*), the steady gauge pressure then assumes a negative value at the central axis $r = 0$ and the steady disk deformation varies non-monotonically with radial distance, both in qualitative congruence with the experimental measurements reproduced in figure 2(*b*) (Weston-Dawkes *et al.* 2021). The disappearance of the first nodal region indicates that the collection of sand on the disk at $r/a \approx 0.3$ observed by Weston-Dawkes *et al.* (2021) may not constitute a Chladni pattern, as the authors suggest, and owes instead to gravity-driven transport toward the valley formed by the mean disk deformation. Interestingly, in the limit of strong coupling $\mathcal{C} \gg 1$, considered separately in Appendix B, the flexural wavenumber of the disk is found to scale with $\mathcal{C}$, in place of the elastic wavenumber K that applies for $\mathcal{C} \sim 1$, and the steady gauge pressure is seen to relax sharply from a negative value at the centre of the film toward zero across a small region $r/a \lesssim 5/\mathcal{C}$. For strongly coupled systems, reducing the degree of coupling $\mathcal{C} \propto 1/\sqrt{h_o}$ thus widens this central region, as observed by Weston-Dawkes *et al.* (2021) during the pull-off process.

For each of the operating conditions depicted in figure 3, the analytical predictions of the time-averaged pressure distribution and disk deformation are confirmed with use of a finite-difference solution of the governing equations (2.14) and (2.15), results of which are visualized in the form of dots and circles in figures 3(*d–f*). As can be seen, for the moderately small relative amplitude $\varepsilon = 0.1$ used in the integration, the numerical solutions display satisfactory agreement with the asymptotic results. The governing equations were discretized with use of second-order central-space finite-difference approximations and marched in time asynchronously, the Reynolds equation with a forward-Euler scheme and the Kirchhoff–Love equation with use of a second-order central-difference scheme (Michael 1963; Moin 2010). The system was initialized with ambient pressure throughout the film $p(r) = p_a$, a uniform disk displacement $w(r) = b$ and zero disk velocity $\partial w/\partial t = 0$. Accurate characterization of the disk motion for
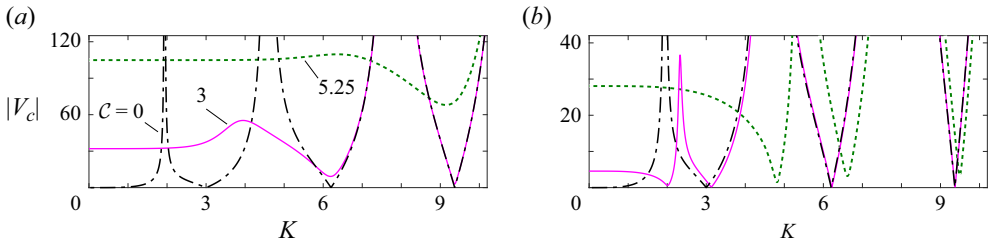
Figure 4. Variation with the elastic wavenumber K of the dimensionless amplitude of the forces modulating the oscillation of a centrally excited disk, as defined in (5.2). Curves are shown for two distinct values of the squeeze number σ – (a) $\sigma = 1$ and (b) $\sigma = 500$ – and compared for states of one-way coupling ($\mathcal{C} = 0$), moderate two-way coupling ($\mathcal{C} = 3$) and strong two-way coupling ($\mathcal{C} > 5$).

$\mathcal{C} \neq 0$ required a sufficiently fine spatial discretization $\Delta\xi = \Delta r/a$ and, in turn, stable convergence to periodicity of the film pressure required a sufficiently small time step $\Delta\tau = \omega\Delta t$. For instance, the solution for $\mathcal{C} = 3$ represented in figure 3(e) was obtained using $\Delta\xi = 0.01$ and $\Delta\tau = 6.3 \times 10^{-4}$. The restriction on the time step for numerical stability generally loosened when increasing the degree of damping; for instance, the solution for $\mathcal{C} = 5.25$ represented in figure 3(f) was obtained using $\Delta\tau = 8.4 \times 10^{-4}$. Note finally that the precise time-averaged shape of the deforming disk $\langle W \rangle$ continued to fluctuate noticeably even after the associated levitation force had converged with a convergence ratio of less than 0.5 %.

7. The attractive load capacity

Based on the results outlined above, it is of great interest to explore the influence of two-way fluid–structure coupling on the attractive load capacity $max(\mathcal{F}_\ell)$ of a flexural squeeze-film system. The asymptotic formulation developed in this study allows analytical determination of the levitation force $\mathcal{F}_\ell$ in the dimensionless form $\mathcal{F}_\ell/(\varepsilon\mathcal{F}_m)$, a measure of system efficiency that takes into account the amplitude $\mathcal{F}_m$ of the supplied excitation force. In principle, the efficiency will be affected both by structural bending forces within the disk and by the evolving overpressure in the squeeze film (see § 2.1). While it is well known that operating near a resonant frequency maximizes the efficiency for one-way-coupled systems ($\mathcal{C} = 0$) due to a weakening of structural impedance and a consequent magnification of the displacement amplitude of points on the disk (Li *et al.* 2014), it is worth exploring here the influence of the additional aerodynamic force that emerges when $\mathcal{C} > 0$. Results are given below in §§ 7.1 and 7.2 for a centrally excited disk ($\xi_c \to 0$), computed using the limiting expressions derived in § 5, and provided in § 7.3 is a sample calculation describing a practical system for which $0 < \xi_c < 1$.

7.1. *Reactive forces that modulate disk oscillation*

Exemplified in figures 4(a) and 4(b) is the variation with the governing parameters of the dimensionless amplitude $|V_c|$ of the oscillatory reactive forces affecting a centrally excited disk, which is evaluated using (5.2). The black dot-dashed curve in each panel, corresponding to a state of one-way coupling $\mathcal{C} = 0$, exhibits zeros for critical values of the wavenumber $K \approx 3.0, 6.2, 9.4, \ldots$, which represent the resonant modes of the flexurally oscillating disk (Warren 1930). As shown in figure 4(a), increasing the strength $\mathcal{C}$ of the aerodynamic forcing tends to uniformize $|V_c|$ for a range of wavenumbers K, thereby eliminating the first few resonant modes. The affected range of K and the number of
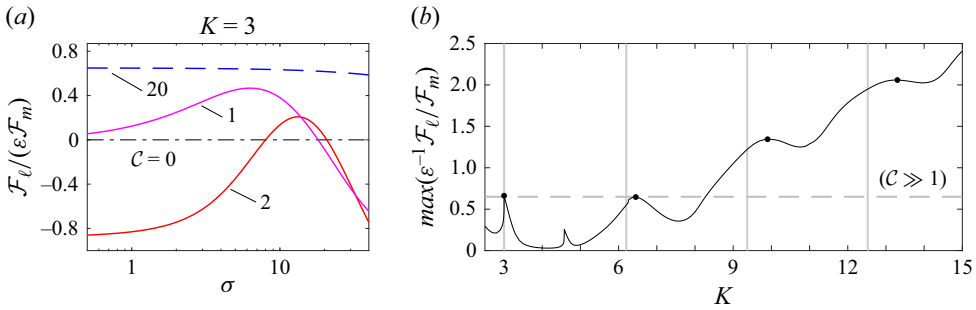
Figure 5. (*a*) Variation with the squeeze number σ and coupling parameter $\mathcal{C}$ of the levitation efficiency (4.8*a*) for a selected value of the elastic wavenumber K. (*b*) Variation with K of the local maximum in efficiency observed for $\mathcal{C} \sim 1$, juxtaposed with the universal value approached for $\mathcal{C} \gg 1$. Vertical lines in (*b*) represent resonant wavenumbers of the undamped disk.

suppressed modes grow as $\mathcal{C}$ is increased. For sufficiently large values of K that satisfy $K^4 \sim \mathcal{C}^6$, the variation of $|V_c|$ gradually returns, in accordance with a restored three-term balance in the Kirchhoff–Love equation (2.15). Noting that $K^4/\mathcal{C}^6 \propto \omega$, this result agrees well with the observed decrease of the damping ratio of flexural squeeze-film bearings for increasing near-resonant operating frequencies ω (Pandey & Pratap 2007). It must be emphasized here that, although $|V_c|$ exhibits local minima of decreasing value as K grows, it never vanishes if $\mathcal{C} > 0$ – the dissipative effect of viscous aerodynamic damping precludes idealistic resonance. The curves in figure 4(*b*) reveal that an increase in the squeeze number σ mitigates modal suppression. The reappearing minima of $|V_c|$ are displaced along the K-axis, with greater displacement occurring for larger values of $\mathcal{C}$, i.e. the shift of the optimal near-resonant frequency $\omega \propto K^2$ increases with the degree of damping, as anticipated for a harmonic oscillator (Zhang *et al.* 2004; Bettini 2016).

7.2. *Parametric dependences of the operating efficiency*

Plotted in figure 5(*a*) is the variation with the squeeze number σ and the coupling parameter $\mathcal{C}$ of the levitative efficiency provided by a centrally excited disk that is oscillating near its first natural frequency, i.e. $K = 3$. The efficiency is computed in the normalized form $\mathcal{F}_\ell/(\varepsilon \mathcal{F}_m)$, with use of (5.6). In practical systems, the value of the elastic wavenumber K is determined by the structural properties of the oscillator and the selected operating frequency, while those of $\sigma \propto 1/h_o^2$ and $\mathcal{C} \propto 1/\sqrt{h_o}$ vary strongly with the evolving separation distance h_o during the pull-off process (see § 2.1 for clarification). Thus, figure 5(*a*) may be interpreted qualitatively to represent the variation of the normalized efficiency with the inverse of the separation distance.

Note first that the efficiency, which scales with $\mathcal{C}^6$ as per (5.6), vanishes in the limit of one-way coupling $\mathcal{C} = 0$ for all values of σ. On the other hand, when $\mathcal{C} = 20$, the efficiency is finite and varies weakly with σ; further computations reveal that this behaviour is found to occur regardless of the value of K, consistent with the observation of modal suppression discussed in § 7.1. In fact, as detailed in Appendix B, in the limit $\mathcal{C} \gg 1$, the efficiency is found to converge to a constant value ≈ 0.6495, independent of both σ and K.

It is apparent from figure 5(*a*) that the efficiency varies non-monotonically with both σ and $\mathcal{C}$, and exhibits a local maximum for a critical combination of the two parameters. Represented in figure 5(*b*) is the value of this extremum, $max(\varepsilon^{-1}\mathcal{F}_\ell/\mathcal{F}_m)$, for various wavenumbers K. The corresponding critical values of σ and $\mathcal{C}$, omitted from the figure for
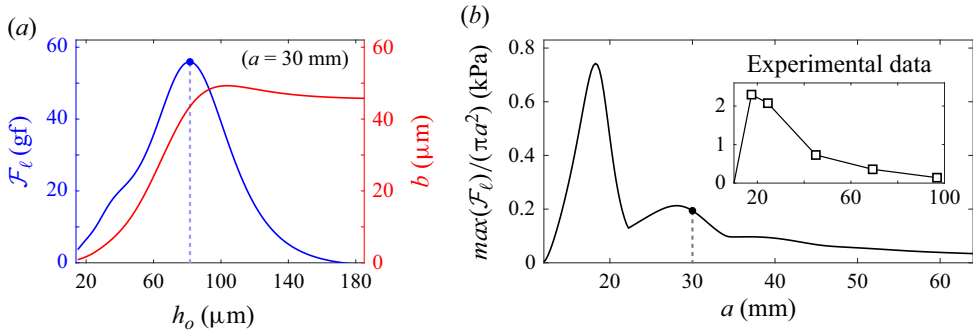
Figure 6. Sample calculations for a disk with thickness $t_d = 150$ μm made of polyester, for which $E_d = 3.65$ GPa, $\rho_d = 1.38$ g cm^{-3} and $\nu_d = 0.48$ (Sasmita *et al.* 2019; MatWeb n.d.), in a gas where $p_a = 101325$ pa, $\mu_a = 1.81 \times 10^{-5}$ kg (m s)$^{-1}$ and $\rho_a = 1.225$ kg m^{-3}. (*a*) Variation with the separation distance h_o of the attractive force $\mathcal{F}_\ell$ and the central oscillation amplitude b, and (*b*) variation with the disk radius a of the area-normalized load capacity, the latter compared with measurements by Weston-Dawkes *et al.* (2021).

clarity, increase nearly monotonically with K. For $K \gtrsim 8.3$, the local maximum exceeds the aforementioned universal value approached in the limit $\mathcal{C} \gg 1$, the latter indicated in the figure by a dashed horizontal line. The curvature of the function $[max(\varepsilon^{-1}\mathcal{F}_\ell/\mathcal{F}_m)](K)$ diminishes as K grows, subsequent peaks which appear for increasing critical values of K, marked by dots, being less accentuated. This suggests a favourable reduction in the sensitivity of the load capacity to the precise excitation frequency (Davis *et al.* 2018) when operating near higher resonant modes. Note, in connection with the concluding discussion in § 7.1, that the critical values of K corresponding to subsequent peaks are increasingly displaced from the respective ideal resonant wavenumbers, the latter represented in the figure by solid vertical lines.

7.3. *Sample calculations for a practical system*

While the squeeze number σ and the coupling parameter $\mathcal{C}$ are formally independent parameters governing the fluid–structure dynamics, during the pull-off process they evolve together as dictated by their respective dependences on the growing separation distance, i.e. $\sigma \propto 1/h_o^2$ and $\mathcal{C} \propto 1/\sqrt{h_o}$. Practical determination of the load capacity $max[\mathcal{F}_\ell(h_o)]$ thus warrants a system-specific calculation, as exemplified below.

Shown in blue in figure 6(*a*) is the predicted pull-off curve $\mathcal{F}_\ell(h_o)$ for an SFL system operating in standard sea-level air under conditions similar to those used in the recent experiments by Weston-Dawkes *et al.* (2021). A vibration actuator with excitation amplitude $\mathcal{F}_m = 74.5$ gf and frequency $\omega/(2\pi) = 200$ Hz is mounted to a cylinder of finite radius $r_c = 10$ mm. The assembly, having an effective mass $m_c = 10$ g, is affixed concentrically to a polyester plastic disk of radius $a = 30$ mm and thickness $t_d = 150$ μm, giving rise to an operating elastic wavenumber of $K \approx 3.75$. As h_o is increased from approximately 15 to 185 μm, the squeeze number and coupling parameter vary respectively from $[\sigma, \mathcal{C}] \approx [10.77, 12.43]$ to $[0.07, 3.54]$. The red curve in the same figure shows the accompanying variation of the central oscillation amplitude $b(h_o)$.

For small separation distances $h_o \approx 20$ μm, the amplitude b vanishes due to augmented aerodynamic resistance ($\mathcal{C} \gtrsim 10$) and the levitation force, which scales with the square of b as seen from (4.8*b*), also decays. Note that this is in stark contrast with the transition to strong repulsion found in systems where effects of two-way coupling on the oscillator dynamics are negligible (Ramanarayanan & Sánchez 2022), i.e. those with

heavier oscillators driven by powerful actuators (Hatanaka *et al.* 1999; Sadayuki 2002; Andrade *et al.* 2020). As the disk is pulled away from the wall, the amplitude rises due to a weakening of aerodynamic resistance and approaches asymptotically a value that is modulated only by structural bending forces within the oscillator. The force $\mathcal{F}_\ell$ also rises and reaches a maximal value $max(\mathcal{F}_\ell) \approx 56$ gf at a distance $h_o \approx 82$ µm, beyond which it decays gradually. In practical systems, displacing the disk beyond the critical distance requires the exertion of a pulling force that exceeds the load capacity $max(\mathcal{F}_\ell)$ and yields, instead, an abrupt failure of levitation, as exemplified in figure 2(*a*). Points on the predicted pull-off curve for distances $h_o \gtrsim 82$ µm thus represent states of unstable equilibria that occur only in experiments involving artificial control of the separation distance (Sadayuki 2002; Yoshimoto *et al.* 2013; Andrade *et al.* 2020).

Furthermore, it is found that the predicted load capacity $max(\mathcal{F}_\ell)$ varies strongly and non-monotonically with the disk radius a. As a is increased from an initial value equal to $a = r_c = 10$ mm, $max(\mathcal{F}_\ell)$ is seen to grow and reach a value of approximately 81 gf when $a \approx 18.5$ mm, before declining and approaching oscillatorily a value of approximately 45 gf when $a \gtrsim 50$ mm. The fact that the variation of the load capacity subsides when a is made sufficiently large is consistent with the aforementioned universal behaviour of the fluid–structure problem in the limit of strong coupling $\mathcal{C}^6 \gg K^4 \sim 1$. The value of the area-normalized load capacity $max(\mathcal{F}_\ell)/(\pi a^2)$ thus collapses when a is increased beyond ≈ 20 mm, as shown in figure 6(*b*). As seen from the included inset, this prediction agrees qualitatively with the observations of Weston-Dawkes *et al.* (2021), who alluded to the possible benefit of increasing the number of oscillators rather than their size when upscaling an SFL system.

In principle, use of the asymptotic formulation introduces relative errors that scale with b/h_o, h_o/a and $h_o^2/(\mu_a/\rho_a/\omega)$, the latter of which is of order unity for this sample SFL system when $h_o \gtrsim 75$ µm. Nevertheless, the scale of forces $\mathcal{F}_\ell$ seen in figure 6(*a*) in the rising portion of the pull-off curve $h_o \lesssim 75$ µm compares favourably with that reported in the experiment (Weston-Dawkes *et al.* 2021) for small distances of order 100 µm, as seen from figure 2(*a*), in stark contrast with the theoretical predictions produced previously with use of a one-way-coupled flow–structure description (Ramanarayanan & Sánchez 2022). It can be anticipated that accurate description of the observed growth of $\mathcal{F}_\ell$ to larger values ≈ 500 gf at greater distances $h_o \approx 2500$ µm, seen in figure 2(*a*), as well as the associated area-normalized load capacities $max(\mathcal{F}_\ell)/(\pi a^2) > 2$ seen in the inset of figure 6(*b*), requires generalizing the present formulation to account for effects of fluid inertia that are non-negligible when $h_o^2 \sim \mu_a/\rho_a/\omega$ (Ramanarayanan *et al.* 2022).

8. Conclusions and recommendations for future work

Developed in this paper is a reduced theoretical description of the oscillatory airflow excited in a slender air layer by the vibration of a compliant bounding surface. This problem of elastohydrodynamic lubrication is relevant to the study of SFL systems that are driven by highly flexible oscillators, which were discovered recently to exhibit attractive load-bearing capacities a thousandfold larger than those driven by stiffer oscillators. Consideration of two-way-coupled fluid–structure interactions is found to provide significantly improved agreement with recent experimental data that revealed (i) a centrally localized distribution of sub-ambient time-averaged pressure within the air layer, (ii) a non-monotonic time-averaged deformation of the disk, (iii) a gradual evolution of the attractive squeeze-film force during the pull-off process and (iv) a non-monotonic variation of the load capacity with oscillator surface area. Summarized below are possible paths for improving the accuracy and utility of the present formulation.

Of primary interest is characterizing the apparent minimum load and the corresponding minimum mean separation distance below which physical contact occurs between the oscillator and the adjacent surface, inducing (i) adverse frictional resistance to lateral motion and (ii) increased noise levels due to the transfer of mechanical vibrations (as noted from personal communication with the authors of Weston-Dawkes *et al.* 2021; Colasante 2022). (Note that such effects may be tolerable or even desirable in contact-based applications such as suction cups, whose vibration has been shown to increase their load capacity (Zhu *et al.* 2006; Hong *et al.* 2009; Wang *et al.* 2010).) Accurate description of the flow–structure physics under such small separation distances may require rigorous characterization of intermolecular forces and surface asperities (Hosoi & Mahadevan 2004; Poulain *et al.* 2022; Rallabandi 2024).

On the other hand, in pursuit of determining accurately the maximum load capacity, the formulation must be generalized to describe (i) nonlinear effects of fluid inertia in the gas layer and its periphery that are no longer negligible under the large separation distances for which the highest attractive forces are measured (Melikhov *et al.* 2016; Ramanarayanan & Sánchez 2022; Ramanarayanan *et al.* 2022), (ii) operational stochasticity for highly flexural and larger-scale systems (Weston-Dawkes *et al.* 2021; Colasante 2023) due possibly in part to hydrodynamic instabilities, (iii) large deformations of the disk that are comparable to its thickness (Timoshenko & Woinowsky-Krieger 1959; Soedel & Soedel 1994), (iv) dissipative effects of structural damping that may be important in describing near-resonant oscillation (Geist & McLaughlin 1994), (v) adverse effects of surface impurities such as cracks and roughness on the load capacity (Weston-Dawkes *et al.* 2021; Colasante 2024) and (vi) hysteresis in the pull-off process due to rapid application of the load (Weston-Dawkes *et al.* 2021). Insights gained by pursuing these avenues of research may also aid the realization and/or improvement of non-axisymmetric SFL configurations, emerging applications of which include low-friction transportation and robotic manipulation (Colasante 2015; Weston-Dawkes *et al.* 2021; Jia *et al.* 2023).

Author ORCIDs.

Ⓑ S. Ramanarayanan https://orcid.org/0000-0002-8968-1118;

Ⓑ A.L. Sánchez https://orcid.org/0000-0003-1349-9843.

Appendix A. Peripheral pressure variations in the lubrication limit

The presumed relaxation condition $p(r = a) = p_a$ introduced in (2.7*a*) implicitly neglects the pressure variations $p - p_a$ existing across the small peripheral region of gas flow that extends for distances of order h_o in all directions from the film edge $r = a$. These variations, which have been shown to provide a non-negligible contribution to the levitation force for systems with order-unity Womersley number $\alpha = [h_o^2 \omega / (\mu_a / \rho_a)]^{1/2}$ (Yoshimoto *et al.* 2013; Ramanarayanan *et al.* 2022), can be neglected in the lubrication limit $\alpha^2 \ll 1$ considered in this study. For a proof, we begin by noting that the disk oscillations induce radial airflow of characteristic speed $u \sim u_c = (b/h_o)\omega a$ in the film, as follows from the balance of volumetric dilation rates in the continuity equation (2.6*a*). A similar analysis of the radial momentum equation (2.6*b*) then provides

$(p - p_a) \sim (\Delta p)_f = (b/h_o)(\mu_a \omega a^2)/h_o^2$ for the characteristic value of the pressure variations along the film. The nature of the flow induced in the small, non-slender periphery depends on the local Reynolds number $Re_p = \rho_a u_c h_o/\mu_a = \alpha^2/St_p$, defined here in terms of the associated local Strouhal number $St_p = h_o^2/(ba)$. On the one hand, though the flow in the film is dominated by viscous forces since $\alpha^2 \ll 1$ (and the Strouhal number in the film, h_o/b, is necessarily greater than unity), inertial forces can dominate in the periphery if $Re_p \gg 1$, i.e. $St_p \ll \alpha^2$. In that case, the associated pressure drop across the periphery $(p - p_a) \sim (\Delta p)_p$ can be expected to scale with the dynamic pressure $(\Delta p)_p = \rho_a u_c^2$, which is negligibly small compared with the pressure variations along the film, i.e. $(\Delta p)_p/(\Delta p)_f = \alpha^2(b/h_o) \ll 1$. On the other hand, in the opposite limit $Re_p \ll 1$, the peripheral flow is also dominated by viscous forces, whence $(\Delta p)_p = \mu_a u_c/h_o$, such that $(\Delta p)_p/(\Delta p)_f = h_o/a \ll 1$. Thus, regardless of the value of Re_p, the pressure drop across the periphery can be neglected when analysing the flow in the film.

The justification outlined above must be reconsidered carefully in the limit of small relative amplitudes $\varepsilon = b/h_o \ll 1$. As mentioned above, when $Re_p \gg 1$, $(\Delta p)_p/(\Delta p)_f \sim \varepsilon \alpha^2$, so that, in the limit $\alpha^2 \ll 1$ considered here, the peripheral pressure variations can be neglected when determining both the leading-order film pressure P_0 and its first-order correction P_1. On the other hand, in the viscous limit $Re_p \ll 1$, $(\Delta p)_p/(\Delta p)_f \sim h_o/a \ll 1$, which can clearly be neglected when determining the leading-order pressure in the film P_0, as done in (3.1). However, deducing the value of $P_1(\xi = 1, \tau)$ requires, in principle, selecting a distinguished limit relating the magnitudes of $h_o/a \ll 1$ and $\varepsilon \ll 1$ and carrying out a formal procedure of asymptotic matching with the peripheral-flow solution (Ramanarayanan *et al.* 2022). Fortunately, this may be avoided in the limit $\alpha^2 \ll 1$ since we are not interested in determining the time dependence of the first-order film pressure P_1. Note that the peripheral variations of density are relatively small, i.e. $(\rho - \rho_a)/\rho_a \sim (\Delta p)_p/p_a \sim \varepsilon \sigma(h_o/a)$, such that the nonlinear effects of gaseous compressibility on the peripheral flow are negligible in the first approximation. For $Re_p \ll 1$, the problem in either flow region is thus linear at leading order. The time-averaged pressure drop, obtained by considering higher-order corrections, exhibits characteristic values of order $\varepsilon(\Delta p)_f$ and $\varepsilon(\Delta p)_p$ along the film and across the periphery, respectively, their ratio remaining therefore of order $h_o/a \ll 1$. Thus, regardless of the value of Re_p, use of the steady relaxation condition $\langle P_1 \rangle(\xi = 1) = 0$ given in (4.1) introduces asymptotic errors consistent with those involved in the general formulation outlined in § 2.2.

Appendix B. Solution for extreme values of the coupling parameter $\mathcal{C}$

B.1. *The limit of one-way coupling $\mathcal{C} = 0$*

The limit of one-way coupling where the disk motion is unaffected by aerodynamic damping, considered earlier for the case of central forcing $\xi_c = 0$ (Ramanarayanan & Sánchez 2022), is described here for $0 < \xi_c < 1$. When $\mathcal{C} = 0$, the Kirchhoff–Love equation (2.15) reduces to $\nabla^4 W + K^4 \partial^2 W/\partial \tau^2 = 0$. Straightforward integration with use of the familiar boundary conditions listed in (2.18) provides $W = S(\xi) \cos \tau$, with

$$S = \begin{cases} 1 & 0 \leq \xi \leq \xi_c \\ \dfrac{J_0(K\xi) + C_1 Y_0(K\xi) + C_2 I_0(K\xi) + C_3 K_0(K\xi)}{J_0(K\xi_c) + C_1 Y_0(K\xi_c) + C_2 I_0(K\xi_c) + C_3 K_0(K\xi_c)} & \xi_c \leq \xi \leq 1 \end{cases}, \quad (B1)$$

where I_m and K_m are the mth-order modified Bessel functions of the first and second kind, respectively. The constant coefficients C_1, C_2 and C_3 in (B1) are given by

$$
\begin{bmatrix} C_1 \\ C_2 \\ C_3 \end{bmatrix} = - \begin{bmatrix} Y_1(K\xi_c) & -I_1(K\xi_c) & K_1(K\xi_c) \\ Y_1(K) & I_1(K) & -K_1(K) \\ \varXi_Y^-(K) & -\varXi_I^-(K) & -\varXi_K^+(K) \end{bmatrix}^{-1} \begin{bmatrix} J_1(K\xi_c) \\ J_1(K) \\ \varXi_J^-(K) \end{bmatrix},
\tag{B2}
$$

involving the auxiliary operator $\varXi_{\mathcal{B}}^{\pm}(x) = \mathcal{B}_0(x) \pm [(1 - \nu_d)/x]\mathcal{B}_1(x)$, where $\mathcal{B}_m$ represents a Bessel/modified Bessel function of order m. Integrating the Reynolds equation (2.14) with use of the known function W provides the pressure P. Expressions for the steady pressure distribution $\langle P_1 \rangle(\xi)$ and the levitation force $\langle F_L \rangle$ generated by arbitrary standing-wave oscillations $S(\xi)$ are provided by Ramanarayanan & Sánchez (2022).

The resonant wavenumbers K of the disk, describing states for which the structural impedance $\mathcal{V}_c$ at the clamp radius $\xi = \xi_c$ vanishes (Warren 1930), are found by solving

$$
\det\left(\begin{bmatrix} J_1(K\xi_c) & Y_1(K\xi_c) & -I_1(K\xi_c) & K_1(K\xi_c) \\ J_1(K) & Y_1(K) & I_1(K) & -K_1(K) \\ \varXi_J^-(K) & \varXi_Y^-(K) & -\varXi_I^-(K) & -\varXi_K^+(K) \\ J_1(K\xi_c) & Y_1(K\xi_c) & I_1(K\xi_c) & -K_1(K\xi_c) \end{bmatrix} \right) = 0.
\tag{B3}
$$

For instance, the first four resonant wavenumbers for a centrally forced disk with a Poisson's ratio $\nu_d = 0.3$ are $K = 3.0005, 6.2003, 9.3675$ and 12.5227. Increasing the clamp radius to $\xi_c = 0.1$ shifts the first mode to $K = 3.0702$, and for $\xi_c = 0.5$, to $K = 4.8155$. Varying ν_d within the range of interest, i.e. $0.3 \lesssim \nu_d \leq 0.5$ (see § 6), has little effect.

B.2. *The limit of strong coupling* $\mathcal{C} \gg 1$

Considered here are centrally forced systems ($\xi_c \to 0$) subject to strong two-way coupling. In the associated limit $\xi_c^{-1} \gg \mathcal{C} \gg 1$, the fluid–structure problem is found to be quasi-steady and independent of ξ_c, $\sigma \sim 1$, $K \sim 1$ and ν_d. The flexural wavelength of the disk scales with $\mathcal{C}^{-1}$, as follows from (3.5), and the magnitude of the squeeze-film overpressure reduces by a factor $O(\mathcal{C}^2)$, as follows from radial momentum conservation (2.6b). The overpressure may thus be expressed with use of the rescaled expansion $\mathcal{C}^2 P = \hat{P}(X, \tau) = \hat{P}_0 + \varepsilon \hat{P}_1 + \cdots$, where $X = \mathcal{C}\xi$ is the aptly rescaled radial distance.

The distribution of time-averaged overpressure can then be expressed in the simplified form $\langle \hat{P}_1 \rangle(X) = (3/2) \int_X^{\infty} \mathrm{Re}\{\hat{\varOmega}\, \mathrm{d}\hat{\varPi}^*/\mathrm{d}X\}\, \mathrm{d}X$, valid for $X > 0$, where

$$
\hat{\varOmega} = \sum_{n=1}^{3}[A_n J_0(\hat{\gamma}_n X) + B_n Y_0(\hat{\gamma}_n X)] \quad \text{and} \quad \hat{\varPi} = \sum_{n=1}^{3} \hat{\gamma}_n^4[A_n J_0(\hat{\gamma}_n X) + B_n Y_0(\hat{\gamma}_n X)]
\tag{B4a,b}
$$

describe the spatial dependence of the leading-order disk deformation $W_0(X, \tau) = \mathrm{Re}\{\hat{\varOmega}(X)\, \mathrm{e}^{\mathrm{i}\tau}\}$ and film pressure $\hat{P}_0(X, \tau) = \mathrm{Re}\{\hat{\varPi}(X)\, \mathrm{e}^{\mathrm{i}\tau}\}$, respectively. Both expressions involve the rescaled roots $\hat{\gamma}_n = \lim_{\mathcal{C} \gg 1}(\gamma_n/\mathcal{C}) = (2^{1/3})(3^{1/6}) \exp[\mathrm{i}(n\pi/3 - \pi/12)]$, for
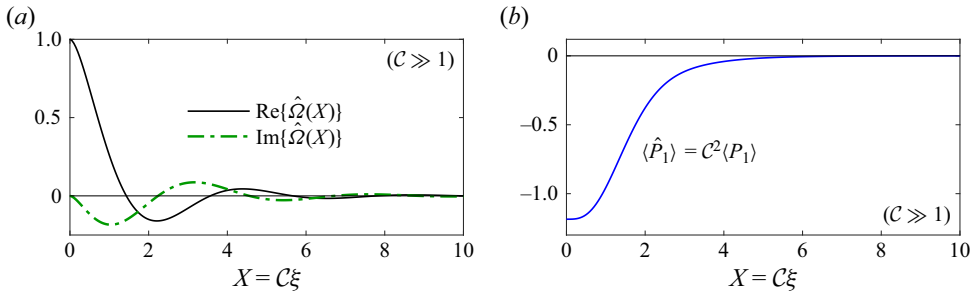
Figure 7. Universal behaviour in the limit of strong coupling $\mathcal{C} \gg 1$: (*a*) components of the travelling-wave disk deformations $W_0 = \mathrm{Re}\{\hat{\Omega}(X)\, \mathrm{e}^{\mathrm{i}\tau}\}$ that are in phase and out of phase with the central oscillations and (*b*) the rescaled time-averaged pressure distribution.

$n = 1 : 3$, and the coefficients $[A_1\ B_1\ A_2\ B_2\ A_3\ B_3] = [1\ 0\ 0\ 0\ 0\ 0]\boldsymbol{M}_\infty^{-1}$, where

$$
\boldsymbol{M}_\infty = \begin{bmatrix} \boldsymbol{V}_1 \\ \boldsymbol{V}_2 \\ \boldsymbol{V}_3 \end{bmatrix}, \quad \text{with } \boldsymbol{V}_n = \begin{bmatrix} 1 & 0 & 0 & \hat{\gamma}_n^{3/2} & \hat{\gamma}_n^{5/2} & \hat{\gamma}_n^{7/2} \\ 2\ln(\hat{\gamma}_n)/\pi & 1 & \hat{\gamma}_n^4 & \mathrm{i}\hat{\gamma}_n^{3/2} & \mathrm{i}\hat{\gamma}_n^{5/2} & \mathrm{i}\hat{\gamma}_n^{7/2} \end{bmatrix} \tag{B5}
$$

for $n = 1 : 3$. Represented in figures 7(*a*) and 7(*b*) are the leading-order disk deformations W_0 and the steady squeeze-film overpressure $\langle \hat{P}_1 \rangle$, respectively, for $\xi_c^{-1} \gg \mathcal{C} \gg 1$.

The dimensionless force $\langle F_L \rangle$ assumes in this limit the simplified form $\mathcal{C}^4 \langle F_L \rangle \approx 4.919$ and the dimensionless amplitude $|V_c|$ of structural impedance at the vanishing clamp radius ($X = \mathcal{C}\xi_c \to 0$) reduces to $\mathcal{C}^{-2}|V_c| \to (2/\pi)|\sum_{n=1}^{3} B_n \hat{\gamma}_n^2| \approx 3.7867$, whence the operating efficiency (5.6) exhibits a constant value $\mathcal{F}_\ell/(\varepsilon \mathcal{F}_m) \approx 0.6495$.

REFERENCES

ANDRADE, M.A.B., RAMOS, T.S., ADAMOWSKI, J.C. & MARZO, A. 2020 Contactless pick-and-place of millimetric objects using inverted near-field acoustic levitation. *Appl. Phys. Lett.* **116** (5), 054104.

BENDER, C.M. & ORSZAG, S. 1999 *Advanced Mathematical Methods for Scientists and Engineers I: Asymptotic Methods and Perturbation Theory.* Springer.

BETTINI, A. 2016 *A Course in Classical Physics 1–Mechanics.* Springer.

BRUNETIÈRE, N., BLOUIN, A. & KASTANE, G. 2018 Conditions of lift-off and film thickness in squeeze film levitation. *J. Tribol.* **140** (3), 031705.

BURROUGHS, M. 2021 Why is vibration amplitude in G? Available at: https://www.precisionmicrodrives.com/why-is-vibration-amplitude-in-g.

CHEN, K., GAO, S., PAN, Y. & GUO, P. 2016 Self-running and self-floating two-dimensional actuator using near-field acoustic levitation. *Appl. Phys. Lett.* **109** (12), 123503.

COLASANTE, D.A. 2015 Apparatus and method for orthosonic lift by deflection. U.S. Patent No. 8967965 B1.

COLASANTE, D.A. 2016 OL5: orthosonic flying saucer. Available at: https://youtu.be/RWUWKx0N_rg.

COLASANTE, D.A. 2022 20in ply CT 34 Hz 60w quiet 40.5lbs!! Available at: https://drive.google.com/file/d/1QPp-9drnPlWl5W4wge4eeMbNE_XyzBu_.

COLASANTE, D.A. 2023 24in x24in AL LFE 15 Hz 200w 436 lbs. net. Available at: https://drive.google.com/file/d/1_2n9Pg3h0cDz-4TFnFCxAi3IVVEM2pTA.

COLASANTE, D.A. 2024 24in x24in LFE 1 mm crack 15 Hz 200w 140 lbs. Available at: https://drive.google.com/file/d/1u_gg3sfhC6pRRfQKyPGGE1cxfPScYc-b.

DA SILVA, F.A.P. 1980 Squeeze film air bearings with flexible supports. PhD thesis, Imperial College, London.

DAVIS, S., GABAI, R. & BUCHER, I. 2018 Realization of an automatic, contactless, acoustic levitation motor via degenerate mode excitation and autoresonance. *Sensors Actuators* A *Phys.* **276**, 34–42.

DUCCESCHI, M. 2014 Nonlinear vibrations of thin rectangular plates: a numerical investigation with application to wave turbulence and sound synthesis. PhD thesis, ENSTA ParisTech, Palaiseau, FR.

FENG, K., LIU, Y. & CHENG, M. 2015 Numerical analysis of the transportation characteristics of a self-running sliding stage based on near-field acoustic levitation. *J. Acoust. Soc. Am.* **138** (6), 3723–3732.

GEIST, B. & MCLAUGHLIN, J.R. 1994 The effect of structural damping on nodes for the euler-bernoulli beam: a specific case study. *Appl. Math. Lett.* **7** (3), 51–55.

GREENWOOD, J.A. 2020 Elastohydrodynamic lubrication. *Lubricants* **8** (5), 51.

GUO, P. & GAO, H. 2018 An active non-contact journal bearing with bi-directional driving capability utilizing coupled resonant mode. *CIRP Ann. Manuf. Technol.* **67** (1), 405–408.

HARRISON, W.J. 1913 The hydrodynamical theory of lubrication with special reference to air as a lubricant. *Trans. Camb. Phil. Soc.* **22** (3), 39–54.

HATANAKA, T., YOSHIKAZU, K., KENTARO, N., SADAYUKI, U. & YOSHIKI, H. 1999 Characteristics of underwater near-field acoustic radiation force acting on a planar object. *Japan J. Appl. Phys.* **38** (11A), L1284.

HONG, Q., LIU, R., YANG, H. & ZHAI, X. 2009 Wall climbing robot enabled by a novel and robust vibration suction technology. In *2009 IEEE International Conference on Automation and Logistics*, pp. 331–336. IEEE.

HOSOI, A.E. & MAHADEVAN, L. 2004 Peeling, healing, and bursting in a lubricated elastic sheet. *Phys. Rev. Lett.* **93** (13), 137802.

ILSSAR, D. & BUCHER, I. 2017 The effect of acoustically levitated objects on the dynamics of ultrasonic actuators. *J. Appl. Phys.* **121** (11), 114504.

ILSSAR, D., BUCHER, I. & FLASHNER, H. 2017 Modeling and closed loop control of near-field acoustically levitated objects. *Mech. Syst. Signal Process.* **85**, 367–381.

JIA, C., RAMANARAYANAN, S., SÁNCHEZ, A.L. & TOLLEY, M.T. 2023 Controlling the motion of gas-lubricated adhesive disks using multiple vibration sources. *Front. Robot. AI* **10**, 1231976.

KELLY, P.A. 2013 Solid mechanics part II: engineering solid mechanics – small strain. Available at: https://pkel015.connect.amazon.auckland.ac.nz/SolidMechanicsBooks/Part_II/index.html.

LANGLOIS, W.E. 1962 Isothermal squeeze films. *Q. Appl. Maths* **20** (2), 131–150.

LI, J., LIU, P. & DING, H. 2014 Dynamic coupling and experimental study on flexural transducer used in near field acoustic levitation. *J. Adv. Mech. Des. Syst. Manuf.* **8** (3), JAMDSM0038.

MATWEB n.d. Overview of materials for polyester film. Available at: https://www.matweb.com/search/datasheet.aspx?matguid=40559706b4fd4aa0a43f5739799728f5.

MELIKHOV, I., CHIVILIKHIN, S., AMOSOV, A. & JEANSON, R. 2016 Viscoacoustic model for near-field ultrasonic levitation. *Phys. Rev.* E **94** (5), 053103.

MICHAEL, W.A. 1963 Approximate methods for time-dependent gas-film lubrication problems. *J. Appl. Mech.* **30** (4), 509–517.

MOIN, P. 2010 *Fundamentals of Engineering Numerical Analysis*, 2nd edn. Cambridge University Press.

OMODIA, I., DAS, K.S. & MAHADEVAN, L. 2022 Vibration-induced elasto-hydro-dynamic adhesion of thin elastic sheet. Poster communication, University of Maryland Eastern Shore and Harvard University.

PANDEY, A.K. & PRATAP, R. 2007 Effect of flexural modes on squeeze film damping in MEMS cantilever resonators. *J. Micromech. Microengng* **17** (12), 2475.

POULAIN, S., CARLSON, A., MANDRE, S. & MAHADEVAN, L. 2022 Elastohydrodynamics of contact in adherent sheets. *J. Fluid Mech.* **947**, A16.

PRECISION MICRODRIVES 2021 Product data sheet: model no. 306-114. Available at: https://catalogue.precisionmicrodrives.com/product/306-114-6mm-vibration-motor-10mm-type.

RALLABANDI, B. 2024 Fluid-elastic interactions near contact at low Reynolds number. *Annu. Rev. Fluid Mech.* **56**, 491–519.

RAMANARAYANAN, S., COENEN, W. & SÁNCHEZ, A.L. 2022 Viscoacoustic squeeze-film force on a rigid disk undergoing small axial oscillations. *J. Fluid Mech.* **933**, A15.

RAMANARAYANAN, S. & SÁNCHEZ, A.L. 2022 On the enhanced attractive load capacity of resonant flexural squeeze-film levitators. *AIP Adv.* **12** (10), 105126.

RAMANARAYANAN, S. & SÁNCHEZ, A.L. 2023 Benefits of controlled inclination for contactless transport by squeeze-film levitation. *Flow* **3**, E26.

ROHSENOW, W.M., HARTNETT, J.P. & CHO, Y.I. (Eds) 1998 *Handbook of Heat Transfer*, 3rd edn. McGraw-Hill.

ROSENHEINRICH, W. 2019 *Tables of Some Indefinite Integrals of Bessel Functions of Integer Order*. University of Applied Sciences.

SADAYUKI, U. 2002 Phenomena, theory and applications of near-field acoustic levitation. *Rev. Acústica* **33** (3-4), 21.

SALBU, E.O.J. 1964 Compressible squeeze films and squeeze bearings. *Trans. ASME J. Basic Engng* **86** (2), 355–364.

SASMITA, F., CANDRA, T.A., JUDAWISASTRA, H. & PRIAMBODO, T.A. 2019 Young's modulus determination of polyester and epoxy by means of ultrasonic pulse echo testing. *IOP Conf. Ser.: Mater. Sci. Engng Des. Appl. Engng Mater.* **547**, 012045.

SHI, M., FENG, K., HU, J., ZHU, J. & CUI, H. 2019 Near-field acoustic levitation and applications to bearings: a critical review. *Intl J. Extrem. Manuf.* **1** (3), 032002.

SIM, K. & KIM, D. 2008 Thermohydrodynamic analysis of compliant flexure pivot tilting pad gas bearings. *Trans. ASME J. Engng Gas Turbines Power* **130** (3), 032502.

SOEDEL, S.M. & SOEDEL, W. 1994 On the free and forced vibration of a plate supporting a freely sloshing surface liquid. *J. Sound Vib.* **171** (2), 159–171.

SONELASTIC n.d. Modulus of elasticity and Poisson's coefficient of polymeric materials. Available at: https://www.sonelastic.com/en/fundamentals/tables-of-materials-properties/polymers.html.

TAYLOR, G.I. & SAFFMAN, P.G. 1957 Effects of compressibility at low Reynolds number. *J. Aeronaut. Sci.* **24** (8), 553–562.

THE ENGINEERING TOOLBOX 2008 Poisson's ratio. Available at: https://www.engineeringtoolbox.com/poissons-ratio-d_1224.html#google_vignette.

TIMOSHENKO, S. & WOINOWSKY-KRIEGER, S. 1959 *Theory of Plates and Shells*. McGraw-Hill.

TULCHINSKY, A. & GAT, A.D. 2016 Transient dynamics of an elastic hele-shaw cell due to external forces with application to impact mitigation. *J. Fluid Mech.* **800**, 517–530.

WANG, W., WANG, K., ZONG, G. & LI, D. 2010 Principle and experiment of vibrating suction method for wall-climbing robot. *Vacuum* **85** (1), 107–112.

WARREN, A.G. 1930 LXXXIII. The free and forced symmetrical oscillations of thin bars, circular diaphragms, and annuli. *Lond. Edinb. Dublin Phil. Mag. J. Sci.* **9** (60), 881–901.

WATANABE, M. & HARA, F. 1997 Theoretical instability analysis of a rotating flexible disk subjected to swirling fluid flow. In *International Mechanical Engineering Congress & Exposition, 4th International Symposium on Fluid-Structure Interactions, Aeroelasticity, Flow-Induced Vibration and Noise*, vol. 2, pp. 57–66. ASME.

WESTON-DAWKES, W.P., ADIBNAZARI, I., HU, Y., EVERMAN, M., GRAVISH, N. & TOLLEY, M.T. 2021 Gas-lubricated vibration-based adhesion for robotics. *Adv. Intell. Syst.* **3** (7), 2100001.

WU, Y., YANG, L., XU, T. & WU, W. 2020 Thermo-elasto-hydrodynamic characteristics analysis of journal microbearing lubricated with rarefied gas. *Micromachines* **11** (11), 955.

YANG, B. 2005 Free vibration of membranes and plates. In *Stress, Strain, and Structural Dynamics* (ed. B. Yang), chap. 16, pp. 807–851. Academic.

YOSHIMOTO, S., SHOU, T. & SOMAYA, K. 2013 Vertical attractive force generated in a noncontact chuck using ultrasonic vibration. *Precis. Engng* **37** (4), 805–811.

ZHANG, C., XU, G. & JIANG, Q. 2004 Characterization of the squeeze film damping effect on the quality factor of a microbeam resonator. *J. Micromech. Microengng* **14** (10), 1302.

ZHAO, S. 2010 Investigation of non-contact bearing systems based on ultrasonic levitation. PhD thesis, Paderborn University, North Rhine-Westphalia.

ZHU, T., LIU, R., WANG, X.D. & WANG, K. 2006 Principle and application of vibrating suction method. In *2006 IEEE International Conference on Robotics and Biomimetics*, pp. 491–495. IEEE.